






# Process Parameter Analysis on Test Structures for the CMS Phase-2 Upgrade Silicon Sensor Production

*Bachelorarbeit eingereicht von* ***Riccardo Dallavalle*** [1]

*geboren am 17.09.1996 in Lecco Italien, verantwortliche Betreuer:*

***Dipl.-Ing. Dr.techn. Thomas Bergauer***

***Dr. Thomas John***

Date: 07.09.2020 Vienna, Austria

[1] dallavallericcardo@outlook.com

**Eidesstattliche Versicherung**

Hiermit versichere ich an Eides statt, dass ich die vorliegende Arbeit selbstständig und ohne Benutzung anderer als der angegebenen Hilfsmittel angefertigt habe. Die aus anderen Quellen oder indirekt übernommenen Daten und Konzepte sind unter Angabe der Quelle gekennzeichnet. Die Arbeit wurde bisher weder im In- noch im Ausland in gleicher oder ähnlicher Form in einem Verfahren zur Erlangung eines akademischen Grades vorgelegt.

Wien, den 7. September 2020

Riccardo Dallavalle

# *Kurzfassung*

Die große Anzahl von Siliziumsensoren, die für das CMS-Phase-2-Upgrade benötigt werden, hat die Entwicklung eines komplexen und genauen Sensor-Qualitätskontrollsystems veranlasst, das die erforderliche physikalische Leistung unter den erwarteten HL-LHC-Bedingungen sicherstellen soll. Ein wichtiger Teil dieses komplexen Systems wird durch die Process Quality Control (PQC) abgedeckt, die in Testzentren in Wien (Österreich), Perugia (Italien), Demokritos (Griechenland) und Brown University (USA) durchgeführt wird. Das Hauptziel von PQC ist es, die Stabilität des Herstellungsprozesses der Sensoren zu kontrollieren und eventuelle Probleme in kürzester Zeit zu lösen. Dieses Bachelorarbeit zielt darauf ab, das PQC-Verfahren zu verbessern und zu verifizieren, indem das am Wiener CMS-Testzentrum HEPHY verwendete PQC Analyseskript weiter entwickelt wurde.

> May the indulgence of the sympathetic reader match the humble feelings with which I present these lines.
>
> *Albert Einstein*
> *The Investigation of the State of Aether in Magnetic Fields*

**Acknowledgments**

## HEPHY

Dedicated to the team of HEPHY for welcoming me with open arms and making me feel at home from the very first moment. A big appreciation goes to Dr. Thomas Bergauer who accepted my proposal to carry out a bachelor thesis at HEPHY. Thanks to Viktoria Hinger for being my mentor and for being such a nice person, your goodness and kindness have been a tremendous blessing to me. Thank you also to my other mentor Dominik Blöch. Viktoria and Dominik, I also have to thank you for the Tuesdays and Thursdays Slack meetings, without which it would have been much harder to complete this project. Thanks also to Marko Dragicevic, Bernhard Arnold and Wolfgang Brandner. Thanks to Peter Paulitisch for his likable character. Thanks to Florian Pitters, Patrick Sieberer, Peter Salajika, Thomas Schwarz. Thanks to Patrick Sieberer for telling me about his stay at CERN as a technical student. Thanks to Nathalie Fortin. I wish you all great success at HEPHY.

## Dr. John, Prof. Dr. Henkel, Prof. Dr. Schmidt

Thanks to Dr. Thomas John, who did everything for me when I first told him about my adventurous project. Thanks for being so available to us on the Integrated Course. Thanks also to Prof. Dr. Malte Henkel for your immense support. Thanks also to Prof. Dr. Thomas Schmidt.

## Others

Thanks to Christina Nelson for teaching me how to do research. For me you are fantastic, a role model of integrity and hard work. Your constructive critiques and improvement tips are imprinted in my mind. Thanks also to Matteo Puel. Also, a greeting to François Corriveau and the whole ATLAS team at McGill University. Thanks also to Helena Reddington for having been my mentor and good friend, you are great. Thanks to my friend Luca Bonamino to share with me the passion for physics. Thanks to Josh Berryman for teaching me how to efficiently use a computer, I wish you the best.

## Author's contribution

The contribution of the author is the development of the PQC analysis script, the results of which are shown in section 4.

## Nomenclature

- ALICE: A Large Ion Collider Experiment
- ASCII: American Standard Code for Information Interchange
- ATLAS: A Toroidal LHC Apparatus
- CERN: Conseil Européen pour la Recherche Nucléaire
- CMS: Compact Muon Soleneoid
- COMET: COntrol and MEasurement Toolkit
- ECAL: Electromagnetic Calorimeter
- fb: femtobarn
- GCD: Gate Controlled Diode
- HCAL: Hadron Calorimeter
- HEPHY: Institut für Hochenergiephysik der Österreichischen Akademie der Wissenschaften
- HGCAL: High-Granularity Calorimeter
- HL-LHC: High Luminosity LHC
- HPK: Hamamatsu Photonics K.K.
- IQC: Irradiation Qualification Centres
- IT: Irradiation Tests
- LCR: inductance (L), capacitance (C), and resistance (R)
- LHC: Large Hadron Collider
- LHCb: Large Hadron Collider beauty
- LINAC2: Linear Accelerators 2
- LS2: Long Shutdown 2
- LS3: Long Shutdown 3
- MOS: Metal-Oxide-Semiconductor
- MOSFET: Metal Oxide Semiconductor Field Effect Transistors
- ÖAW: Österreichischen Akademie der Wissenschaften
- PQC: Process Quality Control
- PS modules: Pixel Sensors modules
- PSB: Proton Synchrotron Booster
- QTC: Quality Test Center
- SMU: Source Measure Unit
- SQC: Sensor Quality Control
- SPS: Super Proton Synchrotron
- TeV: Tera-electronVolt
- 2S: 2 strip sensors modules

# Contents

**Abstract**

The large number of silicon sensors required for the CMS Phase-2 Upgrade has prompted the development of a complex and accurate sensor quality control system, aimed at assuring the needed physics performance under the expected HL-LHC conditions. An important part of this complex system is covered by Process Quality Control (PQC) which is carried out in test centers in Vienna (Austria), Perugia (Italy), Demokritos (Greece) and Brown (U.S.A.). The primary objective of PQC is to control the stability of the manufacturing process of the silicon sensors and to solve any problems in the shortest possible time. This thesis project aims to improve and verify the PQC procedure by developing the customized analysis script used at the Vienna CMS test center HEPHY.
Keywords: PQC, Silicon sensors, HEPHY, CMS, CERN

# 1 Introduction

In order to continue the development of the world's largest particle accelerator at CERN and allow for improved performance, the LHC will undergo maintenance, replacement and development of the elements necessary to run under High-Luminosity conditions. These improvements will be implemented during the LS3 scheduled for 2025. In this context, CMS, one of the two multipurpose particle detectors at CERN, will also undergo an upgrade. In particular, the tracker and the end cap calorimeter will undergo important enhancements to achieve higher granularity and diminish radiation damages. The main components of these two are silicon sensors. The tracker will be entirely silicon and the calorimeter endcap will include 600 $m^2$ of silicon. For this reason, it is necessary to be able to produce a large amount of these in the most efficient and reliable way possible. To this end, the production of silicon sensors is subject to 3 control methods: Sensor Quality Control (SQC), Process Quality Control (PQC) and Irradiation Tests (IT). First, the sensors are tested by the manufacturer Hamamatsu Photonics K.K. (HPK), after which the non-defective sensors are sent to the CMS test centers where they undergo the above-mentioned control procedures: 1. SQC: 10% of the sensors in each batch are irradiated and tested to verify the quality of the silicon sensors. 2. PQC: 20% of the wafers in each batch are tested to verify the reliability and quality of the production processes. 3. IT: 5% of predefined test structures are tested to investigate the functioning of the sensors exposed to high radiation doses, and to see if the behaviour remains stable for all sensors that are produced. Depending on the positive or negative results of these tests it is then decided whether the sensors are suitable to be used for the future upgrade of the CMS detector. This thesis project aims to improve and verify the PQC procedure by developing the customized analysis script used at the Vienna CMS test center HEPHY.

## 1.1 HEPHY

The Institute for High Energy Physics (HEPHY) is Austria's largest center for experimental and theoretical particle physics. It employs more than 70 people and is one of 28 institutes of

the Austrian Academy of Sciences (ÖAW). Located in the city of Vienna, the Institute was founded in 1966 with the aim of conducting research at the European Centre for Particle Physics (CERN). HEPHY makes key contributions to the largest particle physics experiments currently underway, such as the Large Hadron Collider (LHC) in Geneva or the KEK in Japan, and contributes to the future of particle physics through its diverse research activities and innovative developments. HEPHY educates the next generation of physicists by integrating students into its research activities. HEPHY shares its enthusiasm for particle physics with the public through a diverse outreach program [1].

## 1.2 CERN

CERN (Conseil Européen pour la Recherche Nucléaire) is the European organization for nuclear research. It was founded in 1954 with the aim of creating an international research center for nuclear physics. Today, the focus is mainly on research in the field of particle physics. Many important discoveries have been made at CERN, such as the discovery of the W and Z bosons. An important breakthrough was the discovery made in 2012 by the CMS and ATLAS experiments of the Higgs boson, a fundamental element of the standard model. The research that is conducted at CERN has also positive implications on the whole society. The engineering developments used for the LHC are now used for the cure of diseases such as tumors. The austrian MedAustron uses Iontherapy to kill cancer cells sparing more of the surrounding healthy tissues compared to an X-rays treatment [2]. The four main experiments at CERN are: ALICE, ATLAS, CMS and LHCb.

## 1.3 The LHC

The LHC is the biggest particle accelerator at CERN. There, hadrons such as copper ions and protons are made to collide. These particle accelerators provide sufficient momentum to the hadrons to allow the study of particles with minuscule wavelength ($\lambda = \frac{h}{p}$). The LHC is a 27 km large ring. It is situated under the border between France and Switzerland. CMS is one of the detectors placed at one of the four hadrons collision points in the LHC. As can be seen in Fig. 1, protons need a certain energy before entering the LHC. To achieve the required energy, a system of smaller accelerators is used. First, the protons are extracted from hydrogen gas and accelerated to 50 MeV in LINAC2 (LINear ACcelerators 2). Then, PSB (Proton Synchrotron Booster) and PS (Proton Synchrotron) raise the energy to 25 GeV. In SPS (Super Proton Synchrotron), energy reaches 450 GeV. Finally, the protons enter the LHC where they run in opposite directions along two parallel beamlines at 6.5 TeV. At the end of the acceleration stages, they collide at a center of mass energy of 13 TeV. The proton beams are kept on track by a system of magnetic dipoles. These dipoles generate a magnetic field of 8 T which acts on the charged protons allowing them to follow the ring trajectory (Lorentz Force). A system of quadrupoles maintains the beam focused. Before the collision, the beam is focused by a system of higher-order multi-poles. To assure that this magnetic focusing system is working optimally the magnets are kept at low temperature. This is done by a cryogenic ring of liquid helium which surrounds the magnets, thus cooling them.

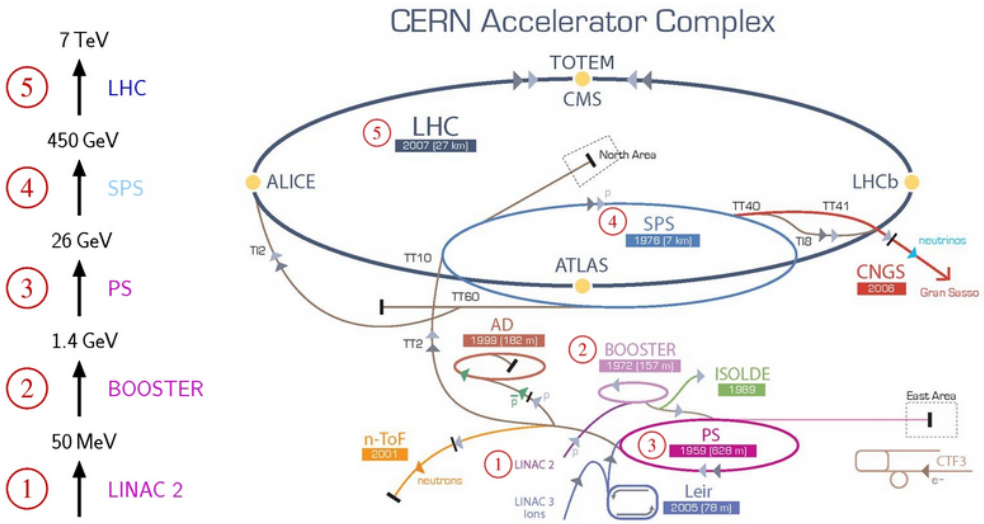


**Fig. 1.** System of particle accelerators at CERN. The LHC is the largest accelerator ring. Before entering the LHC, the proton beams are accelerated in smaller accelerators: LINAC2, PSB, PS and SPS [3].

## 1.4 Proton Beams

As can be seen in Fig. 2, protons in the LHC travel in bunches. They are accelerated by radio-frequency cavities. Each beam is made up of 2808 bunches each separated by 25 ns. Every bunch contains $\sim 10^{11}$ protons. When the beams travelling in opposite directions reach the collision point, the bunches collide. This moment is called bunch crossing. Only a tiny amount of protons will collide. A way to think of this is comparing it to smashing two fistfuls of sand against each other. Most of the grains of sand will miss each other and only a few will collide. The same happens in the LHC. Just 25 protons per bunch crossing will scatter. Most of these collisions produce uninteresting events, which constitute the so-called background.

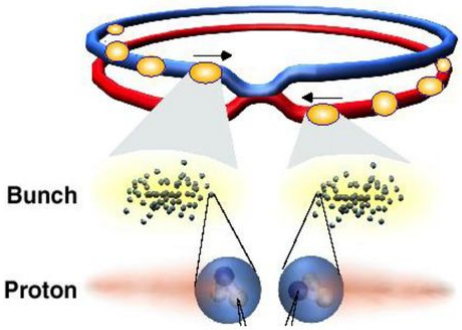


**Fig. 2.** Schematic representation of bunches of protons colliding in the LHC. Only a few collisions produce interesting events that are being selected for analysis [4].

## 1.5 CMS

The Compact Muon Solenoid CMS, Fig. 3, is a multi-purpose detector. It is useful for the study of collisions and the research of new physics. The other multi-purpose detector of the LHC is ATLAS (A Large Toroidal LHC Apparatus). ATLAS uses a different technology than CMS. These two detectors allow a double confirmation, which, in the case of the discovery of a new physics, increases the statistical significance of the results and decreases the systematic error. CMS has a layered structure, each layer performs a particular function. At the edges of CMS, there are endcaps. CMS measures the charge, the momentum, the energy and the vertex interaction of the particles emerging from the collisions. With the relativistic formula that links energy and momentum:

$$E^2 = (pc)^2 + (m_0c^2)^2 \tag{1.1}$$

the rest mass $m_0$ can be calculated and then the type of particle can be determined. CMS has a diameter of 15 m and a length of 28.7 m. The name Compact Muon Solenoid (CMS) originates from its relatively Compact size (e.g. ATLAS has a 10 meter larger diameter). Muon is due to the fact that the reconstruction of muons is optimal and the term Solenoid comes from the fact that there is a solenoid that produces 3.8 T of magnetic field parallel to the beam direction.

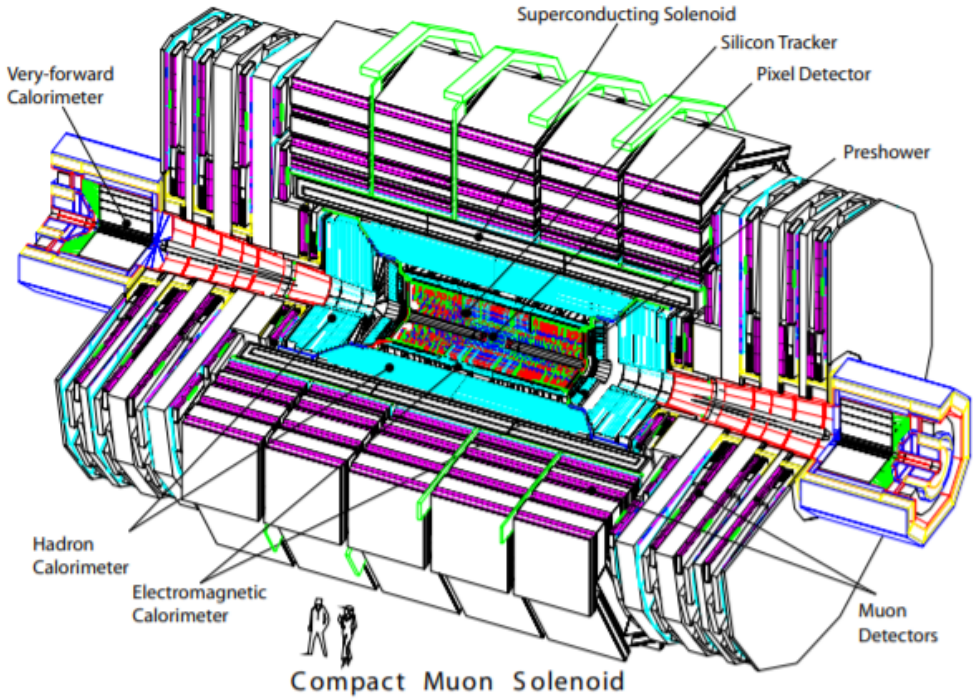


**Fig. 3.** A perspective view of the CMS detector. CMS is 21 meters long, 15 m in diameter, and weights ∼14,000 tonnes [5].

### 1.5.1 Coordinate system

As can be seen in Fig. 4, the interaction point is the origin of the coordinate system in the CMS detector [6]. The z-axis points along the beamline. The y-axis points upwards. The x-axis points towards the center of the LHC ring. The x-y plane is described in polar coordinates by the angle $\phi$ and the y-z plane by the angle $\theta$. Another quantity called pseudo-rapidity, Fig. 5, represents a better coordinate. This has the advantage not to be Lorentz boosted. It is defined as:

$$\eta = \text{-ln tan}\left(\frac{\theta}{2}\right) \tag{1.2}$$

$\eta$ is invariant and thus it is a better coordinate to describe the detector frame.

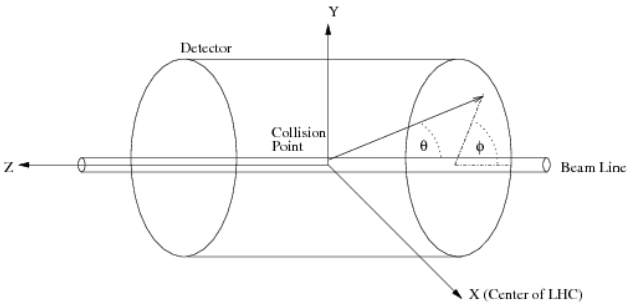


**Fig. 4.** The coordinate system used by the CMS experiment. The origin of the reference frame is the bunches collision point. The z-axis is along the beam-line. The y-axis points upwards and the x-axis points towards the center of the LHC ring [7].

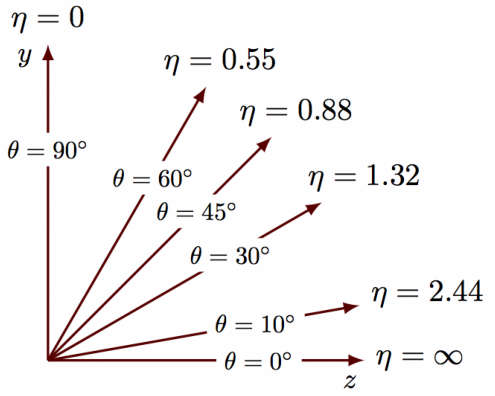


**Fig. 5.** Pseudo-rapidity coordinate as a function of $\theta$. The pseudo-rapidity is a better coordinate to describe the detector environment.

### 1.5.2 Tracking system

The tracker of CMS, Fig. 6, is located at the center of the detector. It is composed of silicon sensors. It is 5.8 m long and has a diameter of 2.5 m and covers a pseudorapidity range of $|\eta| < 2.5$. The task of this tracking system is to measure the path of the particles emerging from the collisions. Then, the momentum of the particles can be determined. The magnetic field generated by the CMS solenoid deflects the trajectory of the particles according to their momentum. The so-called transverse momentum $p_{\mathrm{T}}$ is the component perpendicular to the beam:

$$p_{\mathrm{T}} = p\sin(\theta) = qBR \tag{1.3}$$

where $\theta$ is the polar angle, $q$ is the elementary charge, $B$ is the magnetic field and $R$ is the radius of curvature of the trajectory. The transverse momentum $p_{\mathrm{T}}$ is studied because normally interesting events have particles with a high $p_{\mathrm{T}}$. For this reason, it is important to be able to calculate this parameter precisely. The CMS tracker is divided into inner and outer tracker. The inner tracker is the closest to the beam axis and has a barrel structure with two endcaps at the edges. It is subject to the highest level of radiation density and

therefore its granularity must be very high. That is why pixel sensors with more than 66 million pixels are used. In this way, one can make a precise reconstruction of the vertexes of the decay particle interactions. This reconstruction is done by extrapolating data from the inner and outer tracker. Due to the strong radiation, the inner detector deteriorates very quickly and it is therefore constructed in such a way that the most worn parts can be easily replaced. The outer tracker has a lower granularity since the radiation density itself reduces with distance.

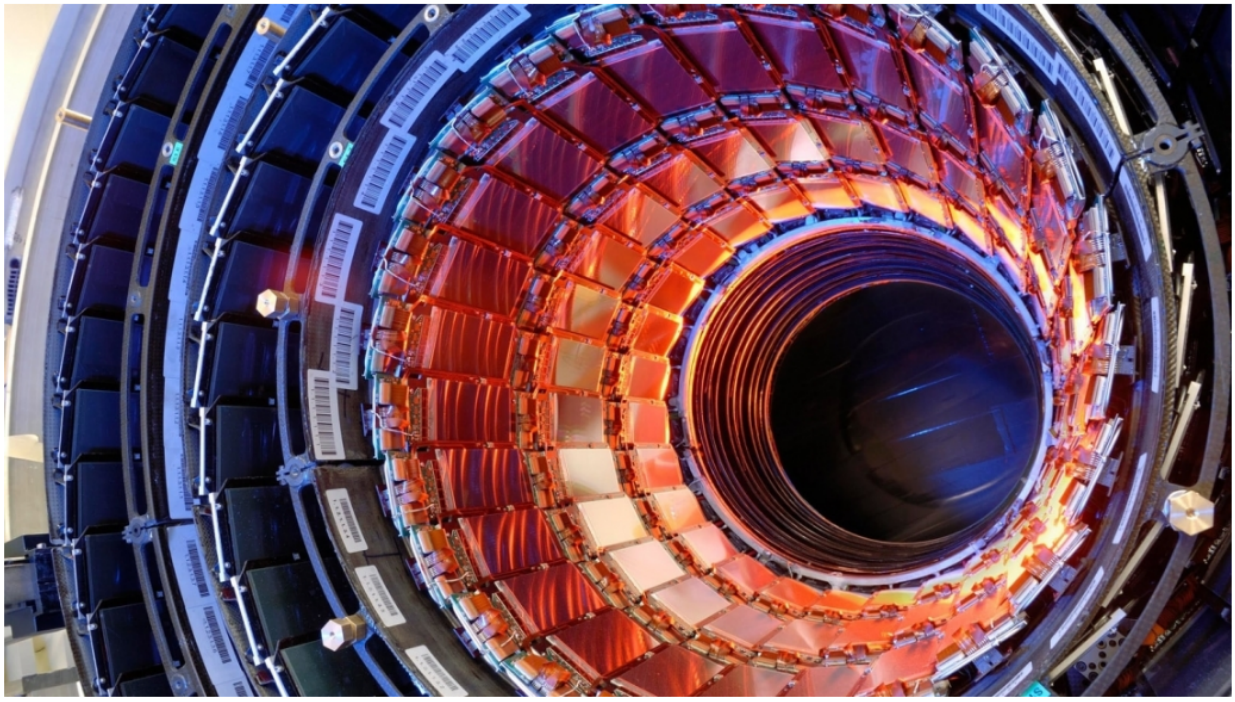

**Fig. 6.** The tracker of CMS is completely made of silicon: pixels, at the very core of the detector, and silicon microstrips detectors around it. When the particles go in the tracker the pixels and microstrips release small electric signals that are detected. The tracker sensors cover a total area the size of a tennis court [8].

### 1.5.3 Calorimeter

The outer tracker is surrounded by the ECAL (Electromagnetic Calorimeter). This measures the energy of particles that interact through electromagnetic force such as photons and electrons. It consists of 68.254 scintillating lead tungstate crystals. The scintillation light of the calorimeter is proportional to the energy of the particle that causes it. Then there is the HCAL (Hadron Calorimeter), which measures the energy of particles interacting with the strong nuclear force. The HCAL is a sampling calorimeter. This means that a hadronic shower occurs in the absorbing layer of the calorimeter and then the energy of the detected particle is derived from the scintillation light of the respective hadronic shower. The internal and external tracker and also the two calorimeters are finally surrounded by the solenoid, which produces the magnetic field of CMS, Fig. 7.

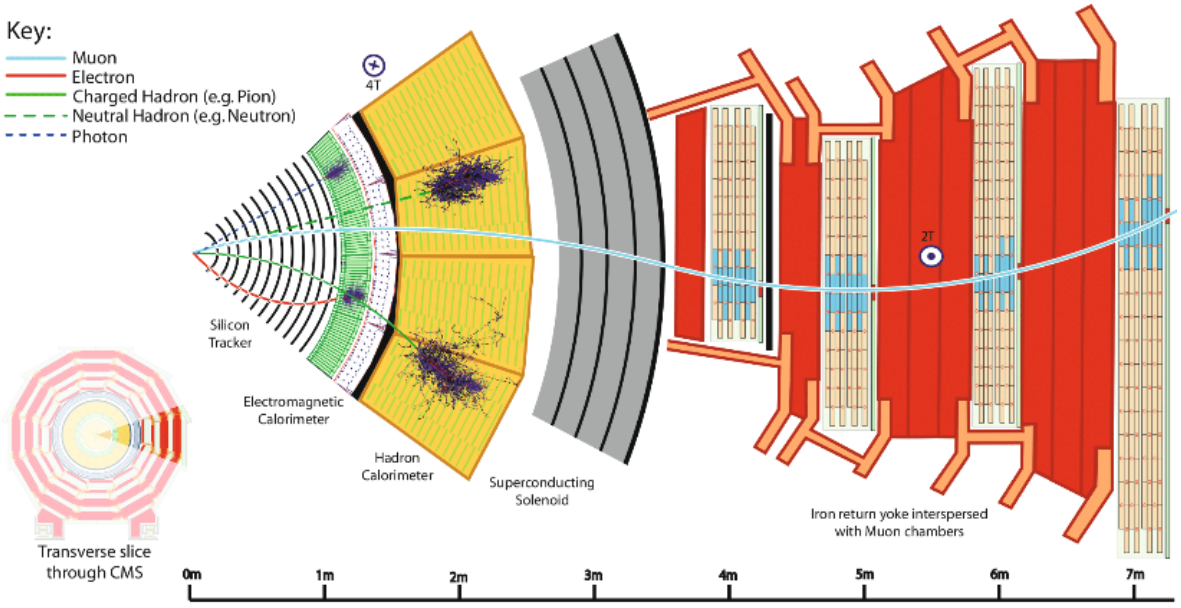


**Fig. 7.** Section of the CMS detector in the projection perpendicular to the beams. The detector has a layer structure. In the innermost layer, tracks of charged particles are detected. A magnetic field perpendicular to the plane of projection causes the tracks to be curved proportionally to $1/p$, making momentum measurement possible. The electrons energy is determined by the electromagnetic calorimeter, which follows as the next layer. Photons behave similarly to electrons in the calorimeter, but they leave no trace in the track system. The stable charged and neutral hadrons lose their energy preferentially in the following hadron calorimeter, with which their energy can also be determined. The following layer is the superconducting solenoid, which generates the magnetic field. The only charged particles that can penetrate all these layers of material are muons. Momentum and direction of muons are measured with track chambers between the iron layers of the magnet return yoke [9].

### 1.5.4 Luminosity

One of the important parameters used to assess the machine performance is called luminosity [10]. The instantaneous luminosity $\mathcal{L}_{\text{inst}}$, evaluates the rate at which collisions happen in the detector. It is a measure of the number of collisions produced per cm$^2$ per second and is calculated as

$$\mathcal{L}_{\text{inst}} = \frac{f\, N_1 N_2}{4\,\pi\,\sigma_x\,\sigma_y} \tag{1.4}$$

Here, $f$ is the frequency of bunch crossing, $N_1$ and $N_2$ are the number of protons in the two colliding bunches, $\sigma_x$ and $\sigma_y$ are the horizontal and vertical components of the cross section of the bunches at the interaction point. The instantaneous luminosity is related to the rate at which any physics process can occur in the detector. If a physics process has a production cross section $\sigma$, then the rate of production $R$ of such a process is $R = \mathcal{L}_{\text{inst}}\,\sigma$. In particular, $\sigma$ is the effective cross-section as the beam profile does not have a sharp edge. A more interesting term useful for physics analysis is the integrated luminosity $\mathcal{L}_{int}$, which

is the instantaneous luminosity integrated over a period of time $t$, and it is defined as:

$$\mathcal{L}_{\text{int}} = \int_0^t \mathcal{L}_{\text{inst}}\, dt \tag{1.5}$$

The integrated luminosity determines the number of events produced in a given data taking period. For a physics process of cross section $\sigma$, the total number of events produced is $N_{\text{events}} = \mathcal{L}_{\text{inst}}\, \sigma$.

## 1.6 High-Luminosity LHC

As can be seen in Fig. 8, the LHC is currently undergoing a long shutdown period of 2-3 years, during which it is being upgraded and maintained. This period is called Long Shutdown 2 (LS2). After this, the Run 3 will begin, and the luminosity will be 2 times higher than the previous Run 2. After Run 3 and during long shutdown 3 (LS3), the upgrade for High Luminosity LHC will be performed. After this upgrade, the integrated luminosity will reach 3000-4000 $\text{fb}^{-1}$ during a period of 10 years. This upgrade will provide an increase in the

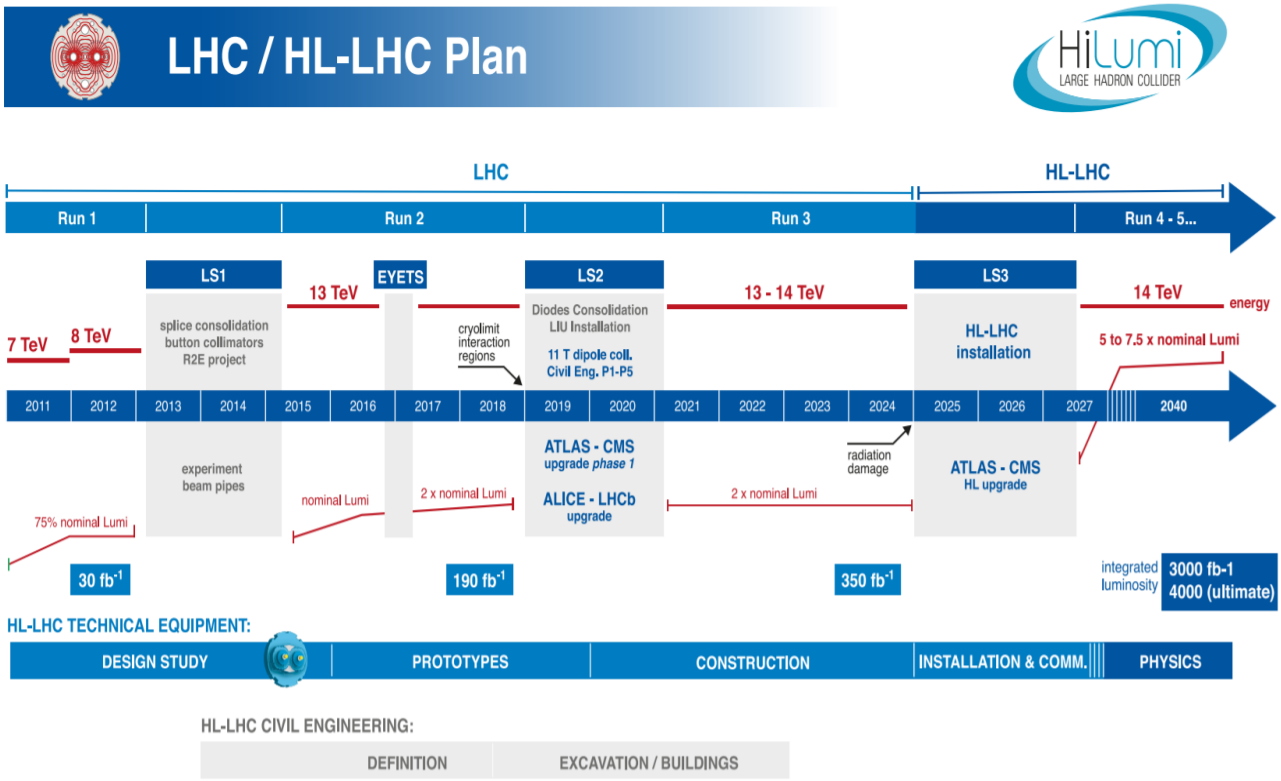


**Fig. 8.** Projected LHC performance until 2035, indicating preliminary dates for long shutdowns of LHC and projected luminosities [11].

available statistics and facilitate the search for a new physics. The CMS physics program at the HL-LHC will build on the experience acquired and the results obtained in the first phase of the LHC operation, with more than 300 $\text{fb}^1$ of accumulated data, and will continue

the quest to answer fundamental questions in particle physics, on one hand with precision measurements, including detailed studies of any new phenomena discovered before LS3, and on the other hand by direct searches for new physics. The study of the Higgs boson will be central to the program [12].

## 1.7 CMS tracker Phase-2 Upgrade

In order to be used during the new High-Luminosity LHC era, CMS will undergo an upgrade during the Long Shutdown 3. This upgrade is called CMS Phase-2 Upgrade. During this period, all CMS components will be upgraded. A new detector technology will be used for the ECAL and HCAL endcaps. A new calorimeter concept will be used, called High Granularity Calorimeter (HGCAL), featuring an area of 600 $m^2$ of silicon sensors.This concept is based on a combination of ECAL and HCAL technologies. The inner and outer detectors will have to be replaced, due to the radiation-damage to the silicon sensors accumulated over the years Fig. 9. Specifically, radiation damage causes the leakage current and the full depletion voltage of the sensors to increase. Therefore, the new tracker is required to be well tolerant to radiation and to be able to support at least an integrated luminosity of 3000 $fb^{-1}$.

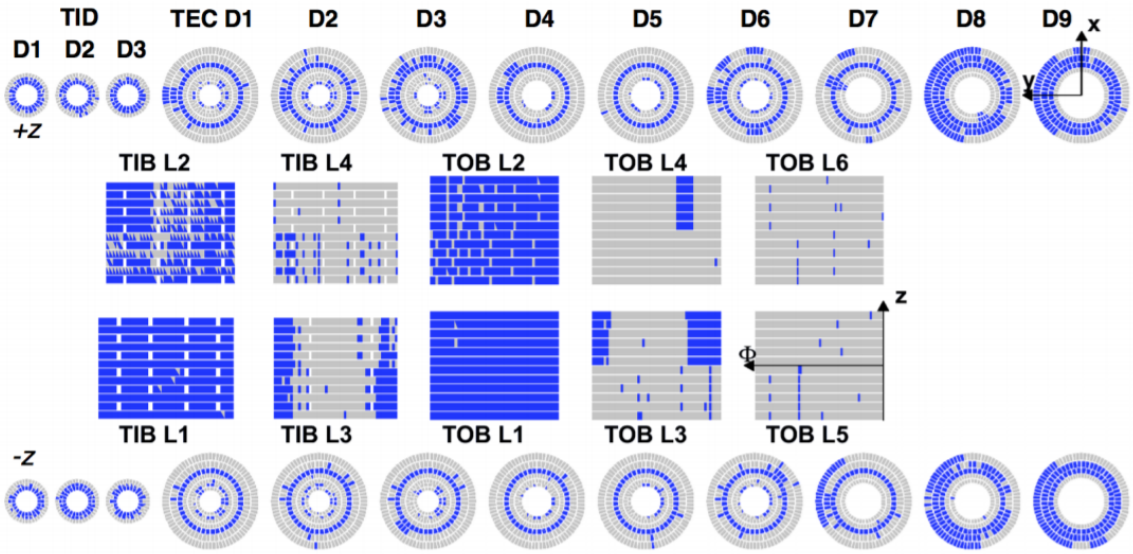


**Fig. 9.** Diagram of non-functional modules (blue) after an integrated luminosity of 1000 $fb^1$ [12]

### 1.7.1 Phase-2 tracker

The new inner tracker, Fig. 10, will use pixel sensors and will have a high granularity, while the new outer tracker will use macro pixels and strip sensors and will have a lower granularity. The new inner tracker will have four layers in the barrel and 12 layers in the endcaps and will cover up to $|\eta| = 4$. It will have an active area 4 times larger than the area of the current tracker. In addition, the components replacement method that was already used for the

previous tracker will also be used for the new tracker. The outer tracker will have 6 layers in the barrel and 5 layers in the endcaps. For the endcaps layers, PS modules and 2S modules will be used. PS modules are composed of macro pixels and strip sensors. 2S modules consist of 2 silicon strip sensors. The PS modules, having a greater granularity, will be placed in the inner part of the outer tracker. In addition, the modules will be placed tilted at an angle along the beam line. This will save the material budget of the new outer tracker while maintaining the same performance as today. The only drawback is the increased complexity of construction.

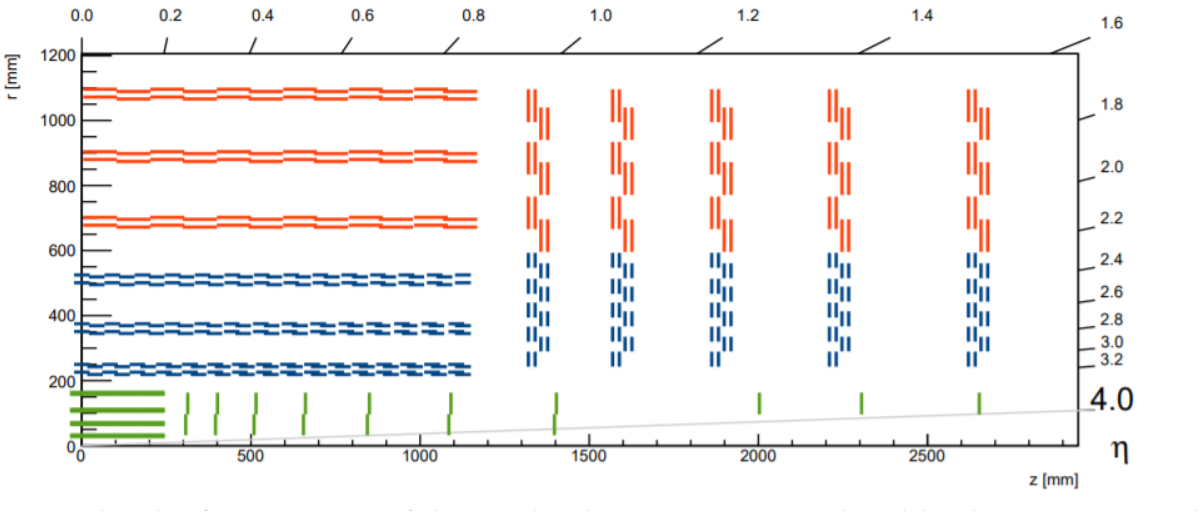


**Fig. 10.** Diagram of one-quarter of the new CMS Tracker. Outer Tracker: blue lines correspond to PS modules, red lines to 2S modules. The Inner Pixel detector is shown in green [12].

## 1.8 High Granularity Calorimeter

To meet the challenges of High Luminosity conditions, the current CMS Endcap calorimeter will be replaced in 2025 by the HGCal (High Granularity Calorimeter), which will comprise: ∼3000 modules containing 620 $m^2$ of Si-sensors, ∼4000 boards containing 400 $m^2$ of scintillators. The new CMS endcap calorimeters, Fig. 11, will feature high density transverse and longitudinal segmentation, which allows fine measurements of electromagnetic showers, taus and jets, even with 5 billion events per second. The HGCal has two main parts: the electromagnetic part (CE-E), which has 28 longitudinal layers equipped with hexagonal silicon sensors and Cu, CuW and Pb integrated absorbers; the hadronic part (CE-H), which consists of 22 longitudinal layers equipped with hexagonal silicon sensors (first 8 layers) or mixed layers comprising silicon sensors and plastic scintillators. Silicon sensors for the electromagnetic part of HGCal will be placed on 60-degree copper plates that serve as mechanical supports and dissipate heat. Sensors are placed on both sides of the support plate to create an assembly called a cassette. Six cassettes are put together to create a single layer of CE-E. Finally, 14 layers of cassettes are stacked together to create a complete CE-E assembly. A single piece of forged aluminum serves as inner support. Hadronic copper plates are split

into 30-degree sectors joined together to create 60- degree cassettes. Unlike CE-E cassettes, Si-sensors are placed only on one side of the support plate and there are 2 types of these cassettes: silicon and mixed (silicon and scintillators). CE-H cassettes are inserted between stainless steel absorbers. The complete CE-H structure consists of 22 layers of cassettes and 23 stainless steel absorber plates. In order to support the 250 tonnes of HGCal weight, supporting wedges are attached to the last absorber. The assembled HGCal is enclosed in a 20 mm thick thermal screen that protects fragile electronics inside the detector.

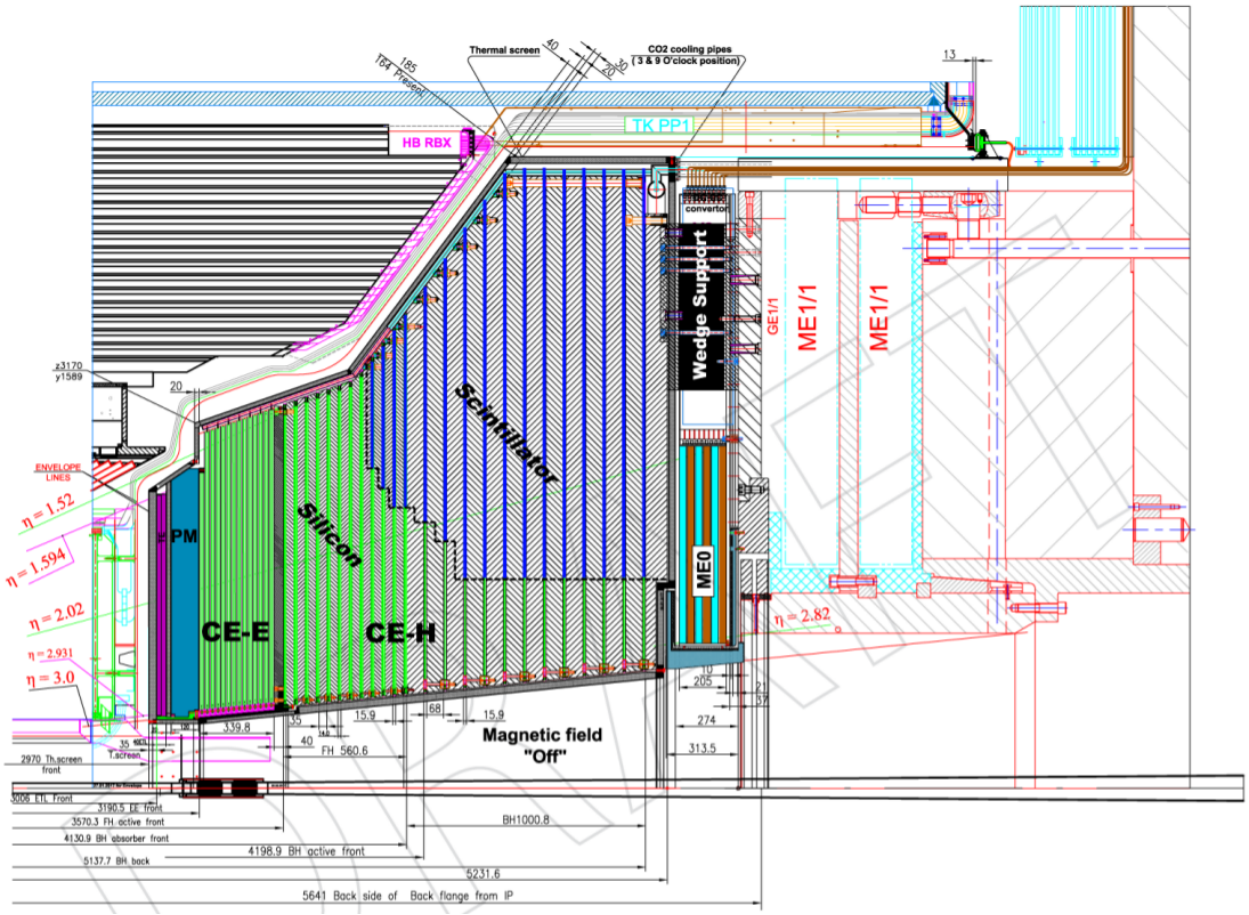


**Fig. 11.** Longitudinal cross-section of the upper-half of one endcap calorimeter [13]

# 2 Semiconductor Physics

Solid materials are divided into three categories depending on the type of band structure, Fig. 12. The insulators have a large bandgap $E_g$, which cannot be occupied by electrons. This is the difference between the conduction band and the valence band. For insulators, the valence band is full and the conduction band is empty. In this case, the thermal energy is not enough to excite the electrons from the valence band into the conduction band. For conductors, the valence band and the conduction band overlap and therefore the thermal excitation of the electrons into the conduction band is possible. Semiconductors have a bandgap that is smaller compared to insulators. Therefore, for temperatures above $T = 0\,\mathrm{K}$, the electrons can be thermally excited into the conduction band leaving holes in the valence band. The example of a semiconductor par excellence is silicon, which is part of the 4th group of the periodic table and has a diamond lattice structure with covalent bonds. Its bandgap energy at $T = 300\,\mathrm{K}$ is $E_\mathrm{g} = 1.12\,\mathrm{eV}$.

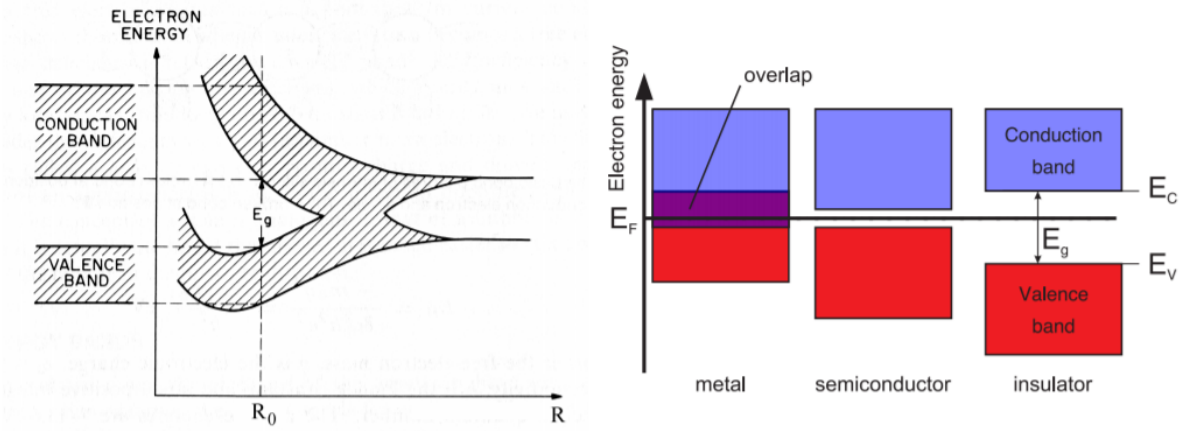


**Fig. 12.** Left: Energy bands in the silicon lattice. The size of the energy bands is defined by the separation distance $R$. The equilibrium separation distance $R_0$ is the silicon lattice parameter $a$. Right: The difference between metals, semiconductor and insulators is simply given by the size of the band gap energy $E_\mathrm{g} = E_\mathrm{C} - E_\mathrm{V}$ [14].

## 2.1 Intrinsic and Extrinsic semiconductors

Intrinsic semiconductors have only small amounts of impurities. For these, the number of free electrons in the valence band $n$, and the number of holes $p$ in the conduction band is equal. This number is also equal to the intrinsic charge density $n_\mathrm{i}$. This can be calculated with the following formula:

$$n_\mathrm{i} = \sqrt{N_\mathrm{C}\,N_\mathrm{V}}\,\exp\left(-\frac{E_\mathrm{g}}{k_\mathrm{B}T}\right) \tag{2.1}$$

where $N_C$ and $N_V$ are the effective density of states of the conduction and valence band. For silicon at $300\,\mathrm{K}$, $n_\mathrm{i} = 9.65\,\mathrm{x}\,10^9\,\mathrm{cm}^{-3}$. For intrinsic semiconductors, the Fermi energy level

is located near the center of the bandgap. A semiconductor is called extrinsic if impurities are introduced into its crystalline lattice. This process is called doping and it changes the physical properties of the semiconductor. As can be seen in Fig. 13, the n-type doping is obtained by adding atoms of the 5th group of the periodic table such as phosphorus or arsenic. Since these have an extra electron, which does not contribute to the covalent bond, this is transferred to the conduction band by adding an energy state to the bandgap near the conduction band. In contrast, p-type doping is obtained by adding atoms of the 3rd group of the periodic table such as Boron. Since these have one electron less than silicon, they are the cause of the creation of holes in the valence band accounting for an additional energy state in the band gap near the valence band. The atoms used for the p-type doping are called donors while those used for the n-type doping are called acceptors. The concentration of doping atoms defines the so-called resistivity of an extrinsic semiconductor. The formula for calculating the resistivity is the following:

$$\rho = \frac{1}{q\,\mu_{\mathrm{n,p}}\,N_{\mathrm{D,A}}} \tag{2.2}$$

where $\mu_{\mathrm{n,p}}$ is the temperature dependent mobility of electrons and holes and $N_{\mathrm{D,A}}$ is the concentration of donors and acceptors.

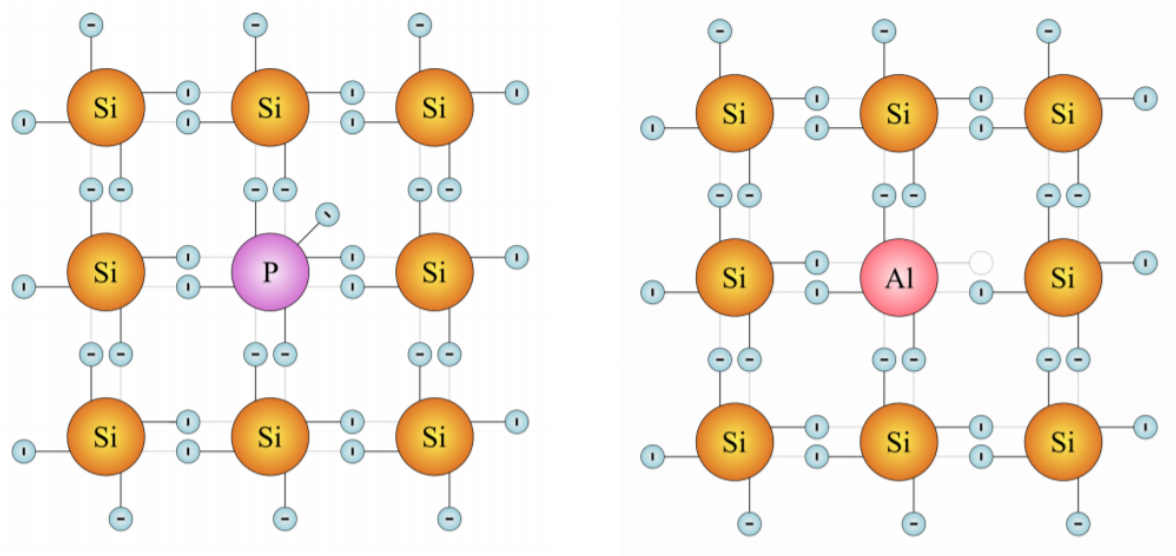


**Fig. 13.** Left: Silicon lattice doped with phosphorus (n-doping). Right: Silicon lattice doped with aluminum (p-doping) [14]

## 2.2 The p-n junction

The p-n junction is also known as diode. As can be seen in Fig. 14, it consists of a contact of p-type and n-type silicon. Due to the different doping in the contact region, the charge carriers start to spread. The surplus of electrons of the n-type silicon spreads towards the holes of the p-type silicon and the holes of the p-type silicon spread to the n-type side of

the junction. This process generates a space charge region because the doping atoms in the vicinity of the junction have lost their neutrality. The expansion of this space charge region is however delimited by the creation of an electric field that slows down progressively the process of diffusion of the charge carriers. The space charge region is also called depletion region because it is depleted of free charges. The width of this depletion region is determined by the doping concentration of n-type and p-type silicon. If the two concentrations are the same, the depletion region will expand equally in the part of p-type silicon and in the part of n-type silicon. One can change the properties of the p-n junctions by applying a bias voltage. Reverse biasing is defined when a negative potential is applied to the p-type region and a positive potential to the n-region. This reverse biasing leads to an increase in the depletion region as the charge carriers move away from each other towards the two electrodes. If one reverses the position of the two electrodes, a so-called forward biasing is generated, whereby the charge carriers move towards each other until there is no longer a full depletion region but rather a current flow. This is the typical behavior of a diode, for which the current can only flow in one direction. Nevertheless, even in the reverse biased configuration, there is always a dark or leakage current. This results from the spread of minority charges in the depletion region, but also from the traps created in the silicon bulks after irradiation.

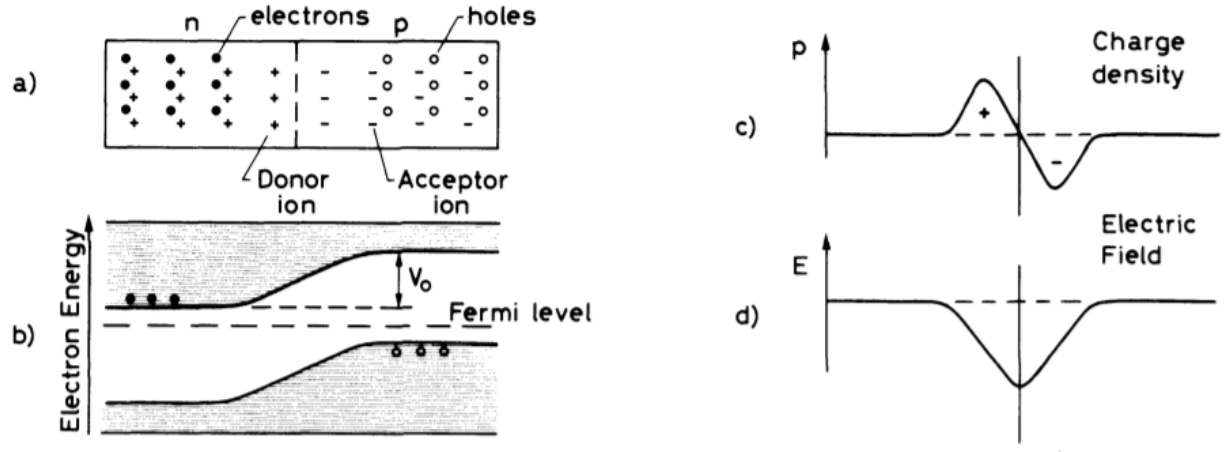


**Fig. 14.** (**a**) Schematic diagram of an n-p junction (**b**) Diagram of electron energy levels showing the potential difference across the junction $V_0$ (**c**) Charge density (**d**) Electric field intensity [15]

## 2.3 Silicon strip sensors

To obtain a fully functional strip sensor, several elements have to be taken into account. The structure of a strip sensor is similar to that of a diode that has been separated into strips at the top. Each of these strips represents a p-n junction. As an example, for a n in p sensor the strips consist of a highly doped n-type area, $n^+$, inserted into a low doped p-type substrate, Fig. 15.

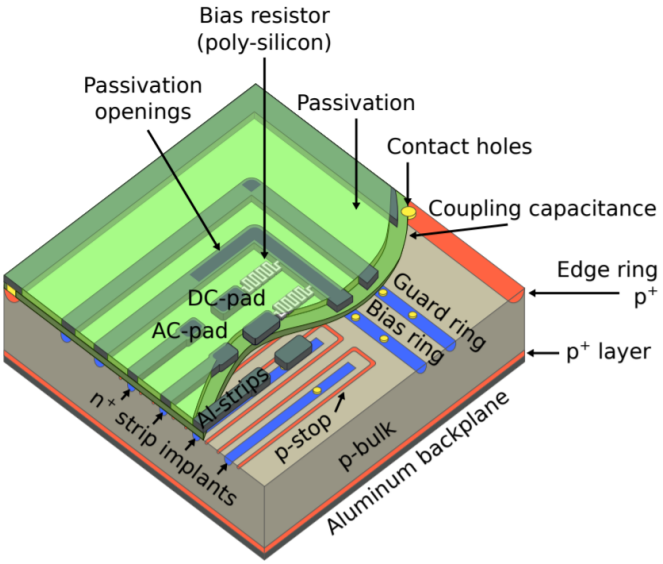


**Fig. 15.** Schematic 3D view of an n in p silicon strip sensor on which the sensor components are distinguished [16]

### 2.3.1 Biasing

To achieve the depletion of a sensor all strips must have the same electrostatic potential and in order to do this, a polysilicon resistor connected to a bias ring is used. This bias ring is common to all strips and therefore all these can be set to ground simultaneously by grounding the bias ring.

### 2.3.2 High voltage stability

To increase the resistance of a sensor to high reversed biased voltages, which could potentially damage it, elements have been introduced into the sensor design. One of the problems, for example, is that when the sensors are cut out from the wafer by a laser or a diamond blade, the sensor extremities could easily be ruined. For this reason, a so-called p+ edge ring has been introduced, which encloses the entire sensor, protecting it from defects due to sawing, which would cause high leakage currents. Furthermore, to reduce the risk of lateral breakdown, an n+ guard ring has been introduced between the edge ring and the bias ring. This ensures a more uniform lateral voltage drop. In addition, a metal overhang can be added with the function to increase strip metallization in order to shift the maximum electric field density above the silicon oxide layer, which has a higher dielectric strength than normal silicon, thus increasing the high voltage stability.

### 2.3.3 Interstrip isolation

There are two ways to ensure interstrip isolation. The first uses a p-spray doping technique, which consists of doping the top layer of the silicon bulk evenly with a $p^+$ implantation. This method does not require an additional production step but increases the risk of high electric fields at the edges of the strips. The other method is to introduce p-stops, i.e. structures

that surround the strips and ensure adequate strip isolation without the risk of high voltages at the ends of the strips. However, this last method requires an additional production step.

### 2.3.4 Protection from environmental influences

To protect the sensor from moisture and mechanical damage and to insulate it electrically, it is coated with a passivation layer. Openings in this layer are made to allow contact with the AC and DC pads and the rings surrounding the strips. This layer can be made of silicon oxide or silicon nitride or even phosphorus silicate glass.

## 2.4 The silicon base material

The essential element for the production of the wafers is silicon. Although silica is one of the most abundant elements in the Earth's crust, pure silicon is very rare to find. That is why the need to produce it. The method of producing very pure silicon is called Float-Zone technique. As can be seen in Fig. 16, a silicon seed crystal is put in contact with a rod of polycrystalline silicon that is subsequently partially melted by a moving heating ring. In this way, the impurities accumulate in the melted part and move together with the ring towards the end of the rod. During the process, the rod rotates on itself so that the temperature can be distributed evenly. The result is an ingot made of a single silicon crystal. The ingot can be doped by adding a gas containing dopant particles in the production process. The ingot is eventually cut into discs that make up the so-called wafers.

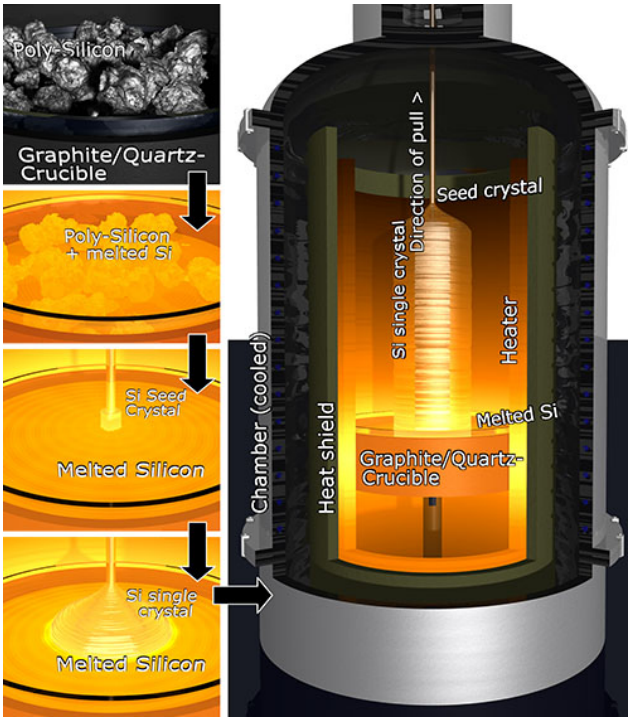


**Fig. 16.** Production scheme of a silicon ingot [17]

# 3 Sensors Characterization - PQC

The large number of sensors prompted CMS to create a quality control procedure to verify that all sensors used by CMS meet the technical specifications. The contract for the construction of the silicon sensors contains a list of tests that must be conducted by the manufacturers and the specific acceptance criteria that must be met. Manufacturers must ensure that at least 99% of the sensors supplied will be able to successfully pass subsequent tests conducted by the CMS Sensor Quality Control (SQC) test centers.

## 3.1 Project overview

The sensors that have been shipped by the manufacturers and then registered at CERN are then forwarded to the Sensor Quality Control (SQC) test centers where they are fully characterized. In particular, the tests conducted by SQC are divided into two types: optical inspection and electrical characterization. The optical inspection consists of a visual check, an inspection with the microscope and a measurement of the characteristic distances of the wafer. During the visual inspection, it is checked if the packaging of the wafers is damaged and if the wafers have obvious damages such as scratches, or an anomalous coloration. After that, the ends of the sensors are checked with the microscope. In fact, the ends are very fragile areas and can easily be damaged due to handling and cutting process and the presence of damages could cause an increased leakage current and an abnormal electrical behavior. Electrical characterization is then performed by means of an automated probe station located in a clean room where temperature and humidity are constantly controlled. This characterization consists of strip by strip tests but also of global tests ($I-V$, $C-V$).

## 3.2 PQC

Test structures undergo a Process Quality Control (PQC) analysis. The PQC analysis is based on test structures that are produced on the same wafers as the sensors, filling the remaining space in so-called half-moons regions (because of their shape). Since these structures are submitted to the same production processes as the sensors, it is possible to use them to perform analyses on the sensor parameters without directly measuring the sensors themselves. The measurement of sensor parameters using test structures saves time and gives the possibility to make measurements that could be harmful if made directly on the sensors. Some test structures are connected to probing systems called flutes, which allow access to the measurements by a probe card. The probe card is then connected through a switching matrix to the measuring instruments (LCR-meter, Source measure units (SMU), Electrometer). The flutes that allow the analysis of the fundamental parameters are named "PQC1" and "PQC2" and it takes about 30 minutes to fully get the measurements from these both flutes. Only the measurement of flutes "PQC1" and "PQC2" at two locations of each tested wafer is foreseen by the standard PQC procedure, this allows for the tracking of process parameter variations across the wafer area. The parameter set is completed by the flutes "PQC3" and "PQC4", which provide access to additional parameters. A measurement of all four flutes takes between one and two hours [18]. Once the measurements are taken, they are then saved as ASCII-files. The file name should include the wafer number, flute

group identifier (Upper-West or Lower-East), flute identifier (e.g. PQC1), structure and measurement type (e.g. Diode-IV, MOS), and the timestamp (UTC) [19].

## 3.3 Irradiation Tests

To verify the adequate radiation hardness of the sensors, irradiation tests are performed using neutrons and protons. Since these are very destructive tests, they are conducted on only 5% of the specific mini-sensors installed in the remaining space on the half-moons. These tests are mainly electrical measurements such as $C - V$ and $I - V$ characteristics and interstrip resistance [20].

## 3.4 Test structures

As can be seen in Fig. 17, test structures are installed on the silicon wafer. These serve to control process parameters that cannot be obtained directly from the strip sensors. In particular, the study of the strip sensors and test structures allows assessment of all relevant process parameters.

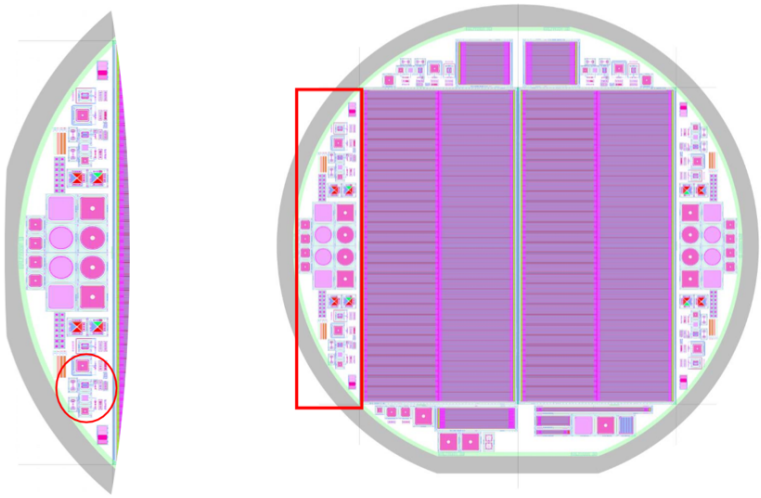

**Fig. 17.** Left: so-called half-moon, on which the set of test structures is installed (red circle). Right: Tracker wafer with two PS-module strip sensors on which the right half-moon is highlighted [21]

## 3.5 Set of test structures

The test structures set, Fig. 18, is composed of a combination of different individual test structures. Test structures are of fundamental importance for the measurement of process parameters. The test structures set is installed at the edges of the wafer, in the region left free by the main sensors. The test structures allow extracting process parameters not otherwise obtainable with the use of main sensors alone and avoid having to make measurements

directly on the sensors, which could be damaged. The individual test structures on the set are connected to flutes that allow the use of a probe card for their accessibility.

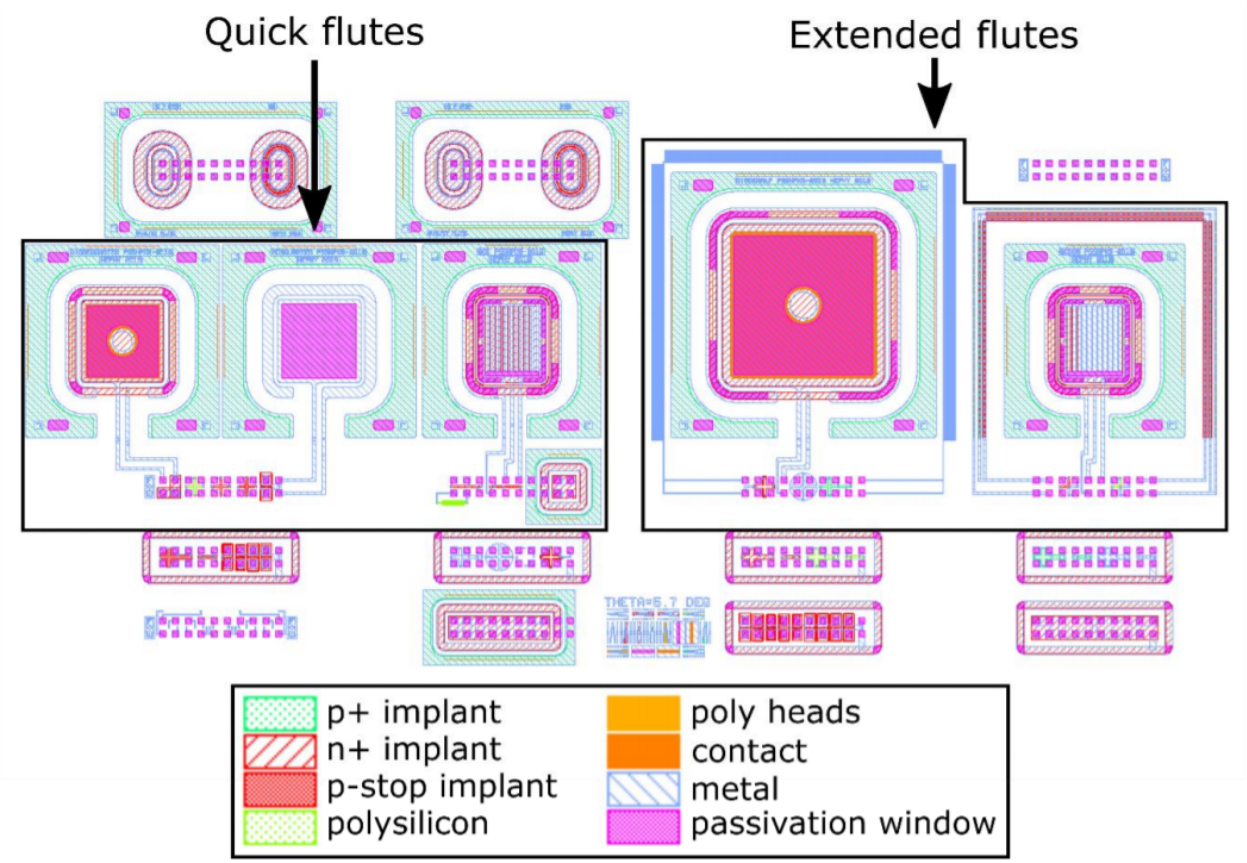


**Fig. 18.** Example of a test structures set. Test structures sets are used to facilitate the extraction of the relevant process parameters [19].

### 3.5.1 Flutes

Flutes are a series of 20 contact pads that are connected to some of the test structures on the wafer. They allow a rapid extraction of the process parameters. For PQC, 15 flutes are used, of which 2 are quick flutes, 2 are extended flutes and the remaining 11 are additional flutes. The quick flutes are measured first because they allow a quick measurement of the process parameters. The extended flutes allow a more in-depth measurement of process parameters and allow verifying the results of the quick flutes. The additional flutes are used for specific measurement of process parameters when needed. The flutes are interspaced in a fixed manner to facilitate automated measurement with a probe card.

### 3.5.2 Diodes

Diodes are used to measure the leakage current and full-depletion voltage. The basic structure of a diode consists of a pad of strip implantation surrounded by a guard ring and an

edge ring. Openings in the passivation layer allow the contact with the center pad, the guard ring and the edge ring. As can be seen in Fig. 19, the standard diode (Diode_Std) has an opening in the metal layer, which allows the induction of a signal using a laser. The diode implemented in the PQC flutes has also an opening in the edge ring, which is done to allow the connection of the diode pad and guard ring to the flute contacts. Thanks to diode structures it is possible to extract the full-depletion voltage, through which one can calculate the bulk resistivity of the wafer (subsection 4.3).

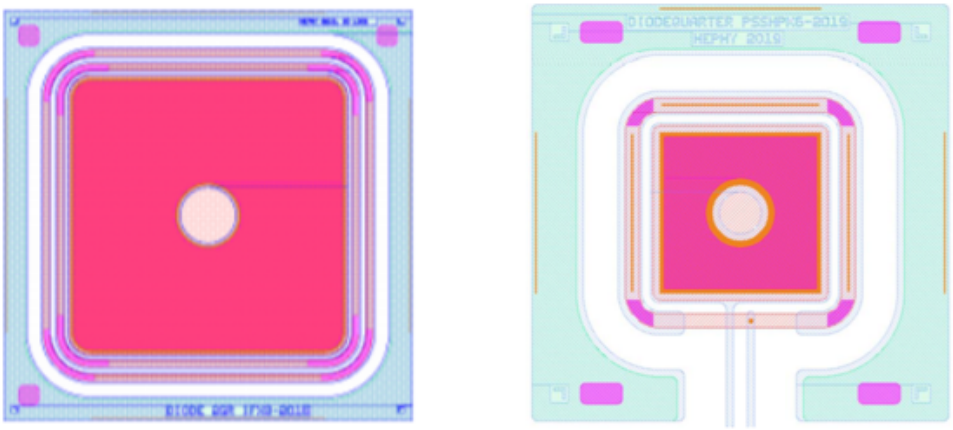

**Fig. 19.** Diode standard on the left. Flute diode on the right [19]

### 3.5.3 Metal-Oxide-Semiconductor test structures

The MOS structure is used to measure the flat-band voltage, the fixed oxide charge concentration and the oxide thickness. In Fig. 20, a Standard MOS and a flute MOS are shown. In Fig. 21, can be seen that the MOS structure can work in three different regimes: accumulation, depletion and inversion. Accumulation is when a negative voltage is applied to the top electrode. The majority carriers accumulate under the gate electrode and the capacitance assumes its maximum value since the dielectric layer thickness of the equivalent plate capacitor is defined only by the thickness of the oxide layer. If one increases the voltage, one reaches the flat-band voltage condition, for which the energy band diagram is flat. That is, the voltage applied to the electrode gate compensates for the electric field created by the fixed oxide charge. If one increases the voltage again, one enters the depletion regime, where the majority carriers are repelled by the electrode gate, creating a space charge region below the oxide layer. The capacitance decreases because the space charge region together with the oxide layer constitute a dielectric layer for the equivalent parellel-plate capacitor. By greatly increasing the voltage, one enters the inversion regime, where the minority carriers of the silicon bulk are pushed towards the oxide layer creating a negative inversion layer. The capacitance reaches its minimum since the space charge region in the silicon bulk has the maximum thickness. The flat-band voltage is determined by the intersection of a linear fit of the capacitance in accumulation with one in depletion. Through the flat-band voltage, it is possible to know the oxide charge concentration, which is important for interstrip isolation,

especially after irradiation (subsection 4.4).

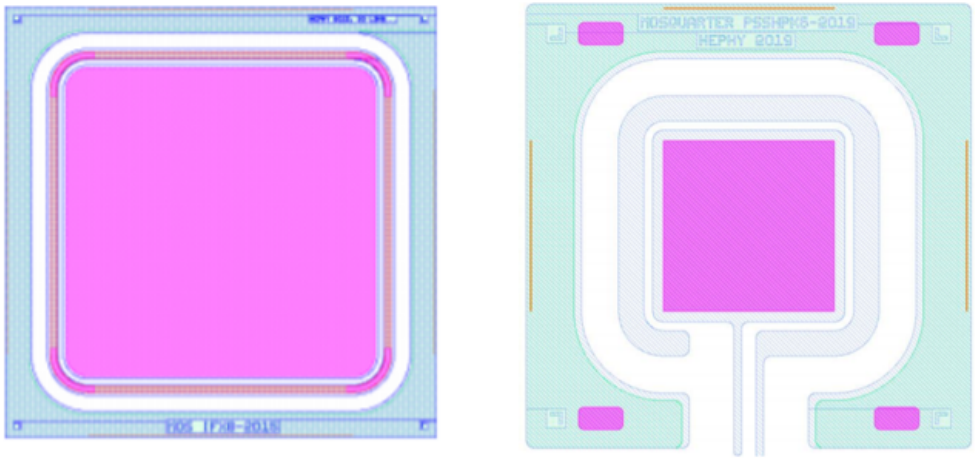

**Fig. 20.** MOS standard on the right. Flute MOS on the left [19]

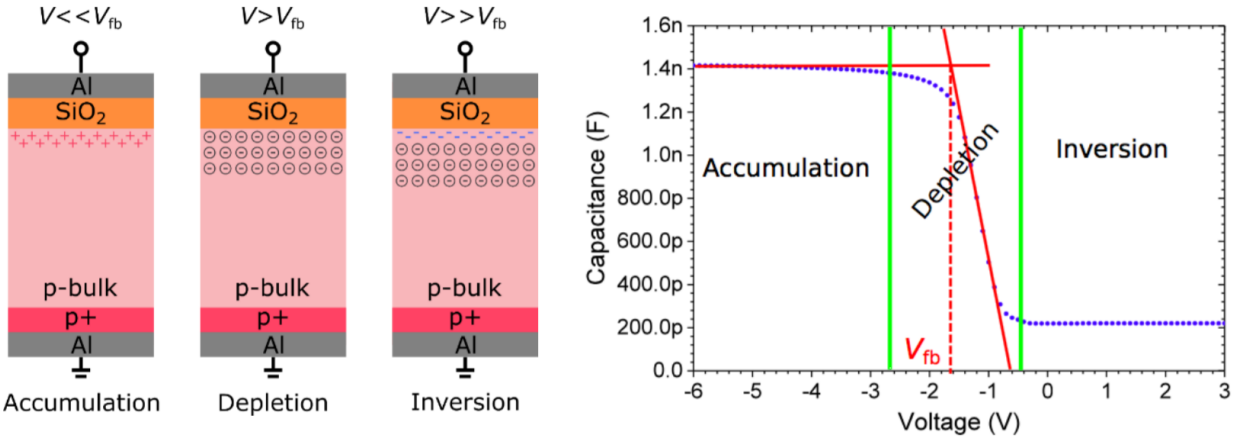


**Fig. 21.** Left: accumulation, depletion and inversion regimes. Right: The flat-band voltage is determined by the intersection of a linear fit of the capacitance in the accumulation regime and a linear fit of the capacitance in the depletion regime [22].

### 3.5.4 Gate Controlled Diode

The Gate Controlled Diode GCD, Fig. 22, is used for the measurement of the surface current $I_{\mathrm{Surf}}$. This last is given by the difference between the current value during inversion and the current value during depletion and is directly proportional to the interface recombination velocity, which is proportional to the silicon oxide interface state density. The GCD is made up of diodes and MOS structures placed next to each other to form a comb structure. The measurement of a GCD requires two voltages, a small and constant reverse bias voltage applied to the implantation region and a voltage applied at the gate electrode. The current

measured at the diode is the superposition of two components $I = I_{\text{Surf}} + I_{\text{b}}$, where $I_{\text{Surf}}$ is the surface current and $I_{\text{b}}$ is the bulk current. The bulk current remains constant, while the surface current changes due to a depletion zone generated below the gate. Three regions can be distinguished: Accumulation: if $V_{\text{gate}}$ is smaller than $V_{\text{fb}}$, only the bulk current is observed. Depletion: if $V_{\text{gate}} = V_{\text{fb}}$ a depletion region below the gate is formed and contributes to the depletion region below the diode. In this regime, there is a sharp increase in the measured current due to the enlarged depletion zone around the MOS region. Inversion: if $V_{\text{gate}}$ is much greater than $V_{\text{fb}}$, there is a sharp drop in current caused by the screening of the surface states by the inversion layer. The current at this point remains constant. Thanks to $I_{\text{Surf}}$, the surface recombination velocity can be extracted and oxide contamination issues may be verified (subsection 4.5).

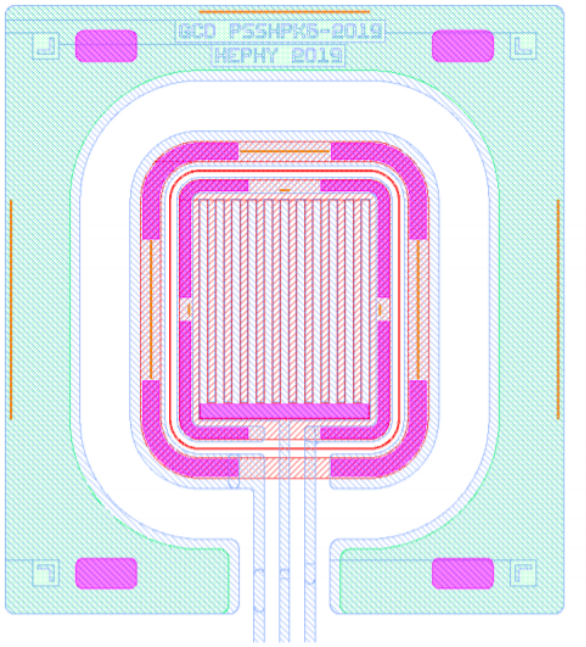


**Fig. 22.** The flute GCD is made of $n^+$ implanted strips together with strips made of MOS material [19].

# 4 Analysis - Results

During the period of this Bachelor's thesis, a Python code IV_PQC.py suitable for the analysis of measurements of process parameters from PQC individual test structures was developed. In particular, the test structures characterized by this analysis are diodes, MOSs and GCDs. The developed code will be useful for a streamlined extraction of test parameters during the PQC process. The whole analysis script can be found on the specific repository in Github [23].

## 4.1 COMET

The GUI shown in Fig. 23, which is used to display the results of the analysis, is called COntrol and MEasurement Toolkit (COMET) [24] and has been previously developed at HEPHY for the SQC analysis. It has been written using the programming language Python. The specification parameters for the different plots (name of the plot, name of the axis, type of plot, type of units, etc.) are stored in a .yml file [25] together with the values of the analysis constant parameters (e.g. elementary charge, dielectric constant, Boltzmann constant).

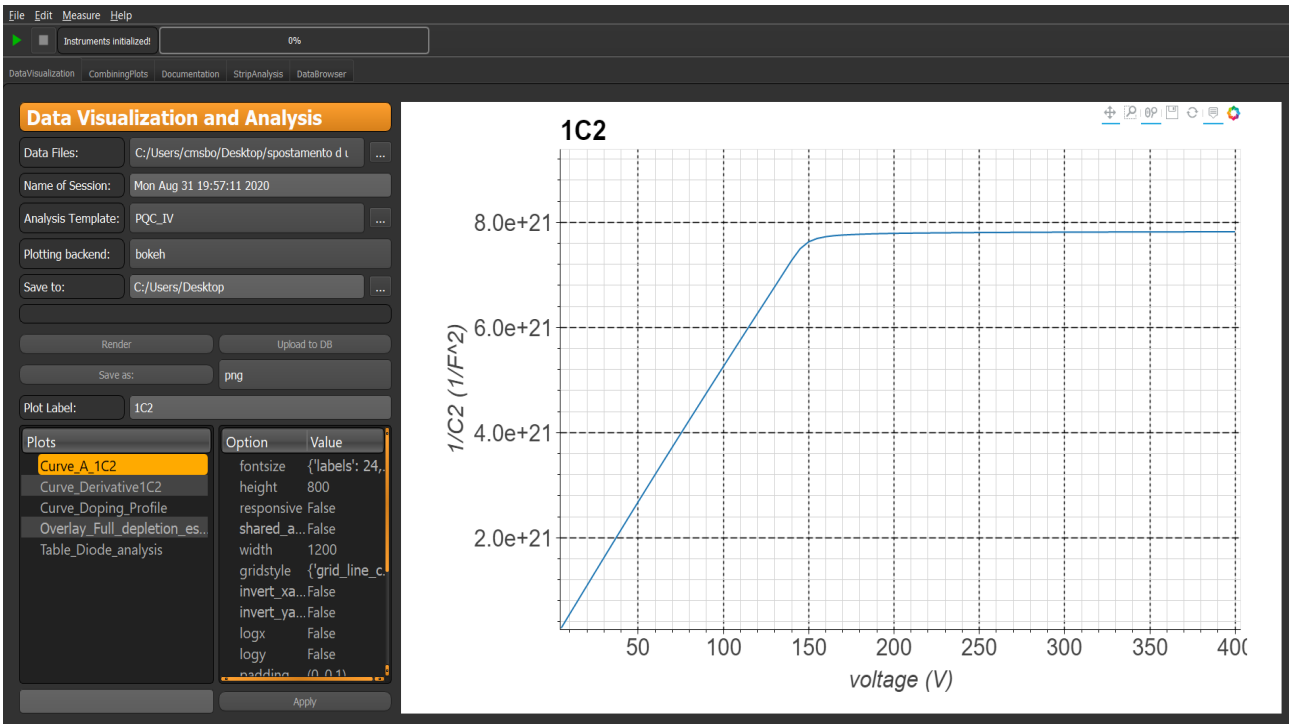


**Fig. 23.** COntrol and MEasurement Toolkit (COMET) user interface

## 4.2 Importer

One needs to specify in the PQC_IV.yml file the path of the importer_PQC.py file. This is a customized importer [26] specific for the PQC files. As can be seen in Fig. 24, it is used to import the data values from the .txt files and sort them based on the type of file (MOS, diode or GCD).

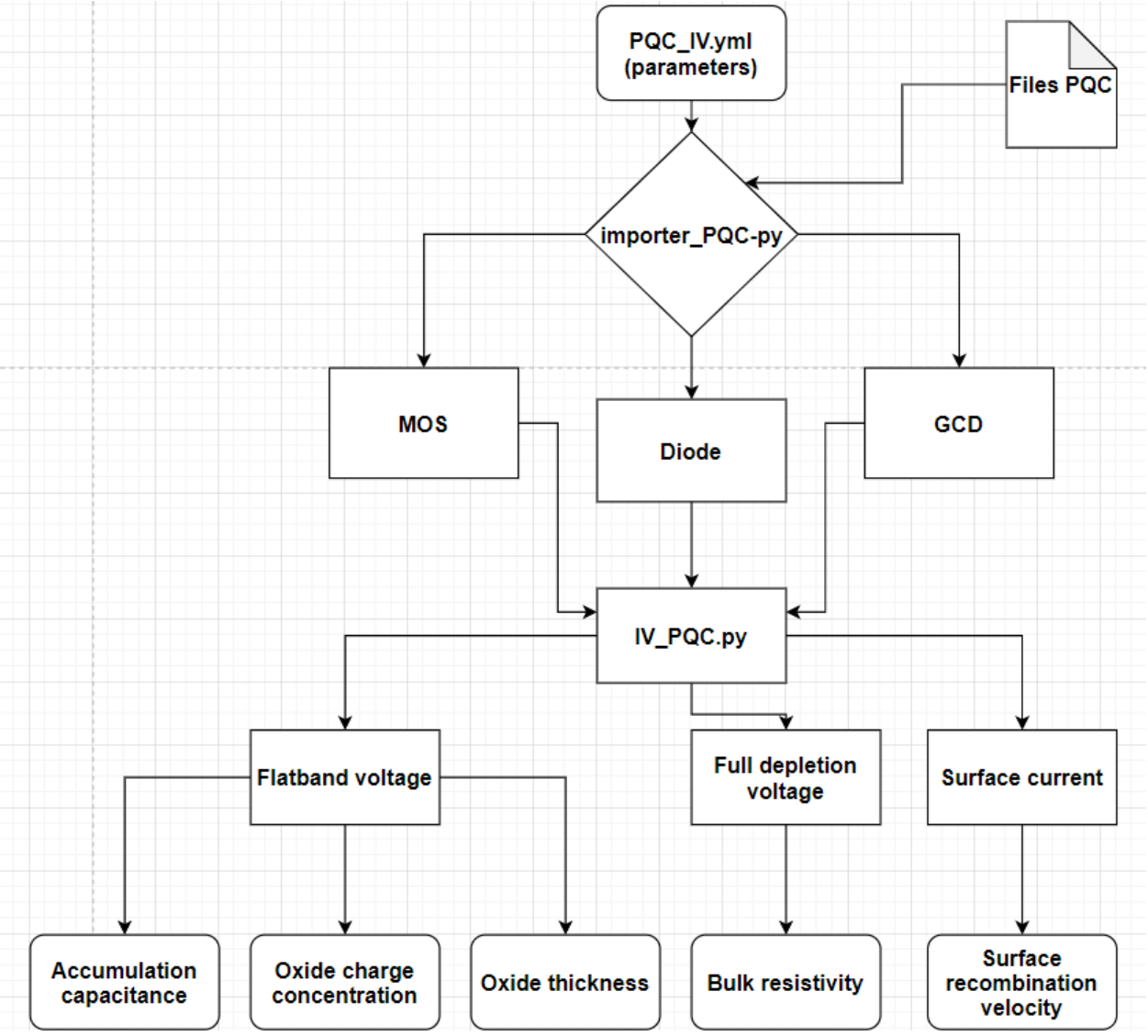


**Fig. 24.** Flowchart description of how the software works. In the parameters file, a customized importer is selected. This extracts the data and decides on which kind of structures they belong. Then the structure-specific analysis is done by the IV_PQC. py code.

## 4.3 Diodes

By means of a diode, one can investigate the full depletion voltage $V_{\text{depl}}$, the doping concentration and the bulk resistivity. The silicon bulk is biased in reverse by a voltage varied between 0 and 500 V, where the capacitance is measured in steps of 5 V. The width of the depletion region in reversed bias is studied through a Capacitance-Voltage curve. In this way, the diode is compared to a parallel-plate capacitor, in which the depletion region constitutes the dielectric between the p-type and n-type silicon plates. This results in a capacitance:

$$C = \frac{\epsilon_0 \, \epsilon_r \, A}{D} \tag{4.1}$$

where $A$ is the electrode area. If one increases the reverse-biased voltage, one also increases the width of the depletion region and consequently the capacity decreases. When the width of the depletion region no longer increases, the diode is said to be fully depleted and this is called the full depletion voltage. At this point, the capacitance assumes its minimum value. Thus, the shape of the $1/C^2$-$V$ curve is linear until the full depletion, and then reaches a plateau [22], Fig. 25. To calculate the full depletion voltage, one looks for the intersection point between two linear fits in the $1/C^2$ versus voltage plot. The first fit is for $V < V_{\text{dep}}$ and the other for $V > V_{\text{dep}}$. The doping concentration (acceptors concentration) $N_{\text{A}}$ can be determined using:

$$N_{\text{A}} = \frac{2}{q_0 \, \epsilon_0 \, \epsilon_r \, A^2 \, \dfrac{d\,(1/C^2)}{dV}} \tag{4.2}$$

The bulk resistivity is calculated as:

$$\rho = \frac{d^2}{2 \, \epsilon_0 \, \epsilon_r \, \mu_{\text{p}} \, V_{\text{depl}}} \tag{4.3}$$

where $d$ is the active sensor thickness of the diode $d = \epsilon_0 \, \epsilon_r \, \dfrac{A}{C_{\text{min}}}$, $C_{\text{min}}$ is the capacitance beyond full depletion, and $\mu_{\text{p}}$ is the holes mobility. As shown in Listing 1, the analysis script for the diode files does the following: First, it calculates the first derivative of the $1/C^2$ curve. Then, it calculates doping concentration $N_{\text{A}}$ and doping profile depth $x(V) = \dfrac{\epsilon_0 \, \epsilon_r \, A}{C(V)}$, where the active area used for the calculations is $A = 26.8\,\text{mm}^2$. After that, it calculates the full depletion voltage as the intersection of two lines, Fig. 26. The first line is traced by considering the slope of the $1/C^2$ curve and fitting it from the left using an algorithm that starts with a fixed number of points from the left of the curve and fits a linear function to it, then adds more points and do the fit again checking whether the R-squared parameter becomes better, keeping only the fit with the best R-squared value, then it takes more points and repeats the process through all points. The other line on the right is simply a horizontal line going through the average of the last 20 values of the $1/C^2$ curve. Finally, the script computes the bulk resistivity.

```
# Compute first derivative of 1/C2
firstdev_invers_C2 = self.build_first_derivative(self.data[df]["data"][
    self.xaxis], self.data[df]["data"]["1C2"])
self.insert_in_df(df, 4, "derivative1C2", firstdev_invers_C2)

# Calculate deep x
x = (self.config['IV_PQC_parameter']['epsilonNull'] * (1e-6) * float(self.
    data[df]['header'][0].split(':')[1]) * self.config['IV_PQC_parameter'][
    'epsilonSiliconOxide']) / self.data[df]["data"]["Capacity"][:42]
self.insert_in_df(df, 5, "x", x) #You can choose also more or less than 42
     data points, depending on how the curve looks like. I used the first
    42 because the end of the curve was oscillating.

# Calculate doping profile
N = (2) / (self.config['IV_PQC_parameter']['epsilonNull'] * (1e-2) \
           * self.config['IV_PQC_parameter']['q'] * self.config['
    IV_PQC_parameter']['epsilonSiliconOxide'] *
           self.data[df]["data"]["derivative1C2"][:42] \
           * (float(self.data[df]['header'][0].split(':')[1]) * (1e-8)) *
    (float(self.data[df]['header'][0].split(':')[1]) * (1e-8)))
self.insert_in_df(df, 6, 'N', N)

[...]

        # Loop one time from the from the left side, to get the slope
        LR2 = 0
        for idx in range(5, len(df)-20):
            # Left
            slope_left, intercept_left, r_left, p_value, std_err_left =
    linregress(df["xaxis"][:-idx], df["yaxis"][:-idx])
            r2_left = r_left * r_left
            self.log.debug("Left side fit: Slope {}, intercept: {}, r^2:
    {}, std: {}".format(slope_left, intercept_left, r2_left, std_err_left))

            # See if the r2 value has increased and store end points
            if r2_left >= LR2:
                LR2 = r2_left
                LeftEndPoints = ((df["xaxis"][0], intercept_left), (df["
    xaxis"][idx], slope_left * df["xaxis"][idx] + intercept_left))

# Find the right fit by averaging on the final 20 points
average_right = np.mean(list(df['yaxis'][-20:]))
RightEndPoints =[(df['xaxis'][len(df['xaxis'])-20], average_right), (df['
    xaxis'][len(df['xaxis'])-1], average_right)]

# Find the line intersection
full_depletion_voltages = line_intersection(LeftEndPoints, RightEndPoints)
```

**Listing 1.** Python code for diode-files analysis

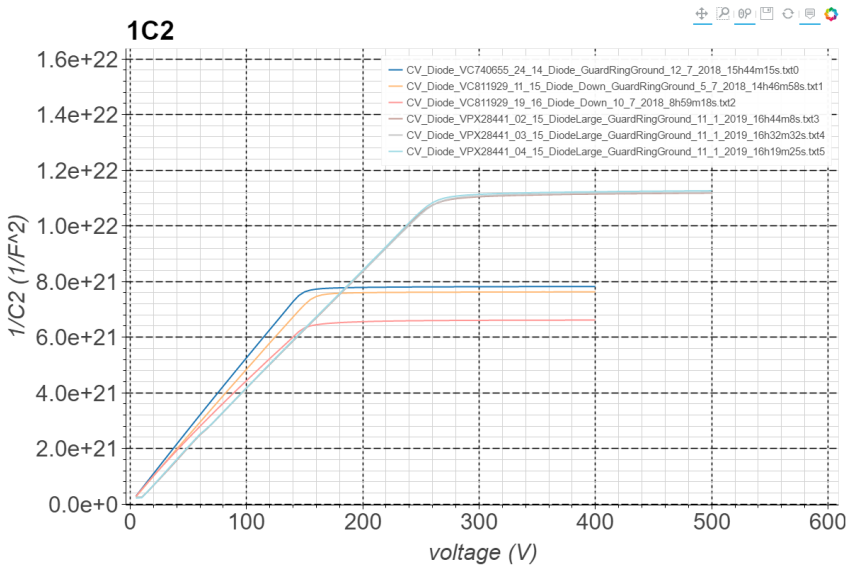


**Fig. 25.** $1/C^2$ curves for different files corresponding to different types of diode. The curves showing a higher full depletion voltage are from diode large-files and they maintain a lower capacitance value after full depletion, this property is related to the different area of the diodes.

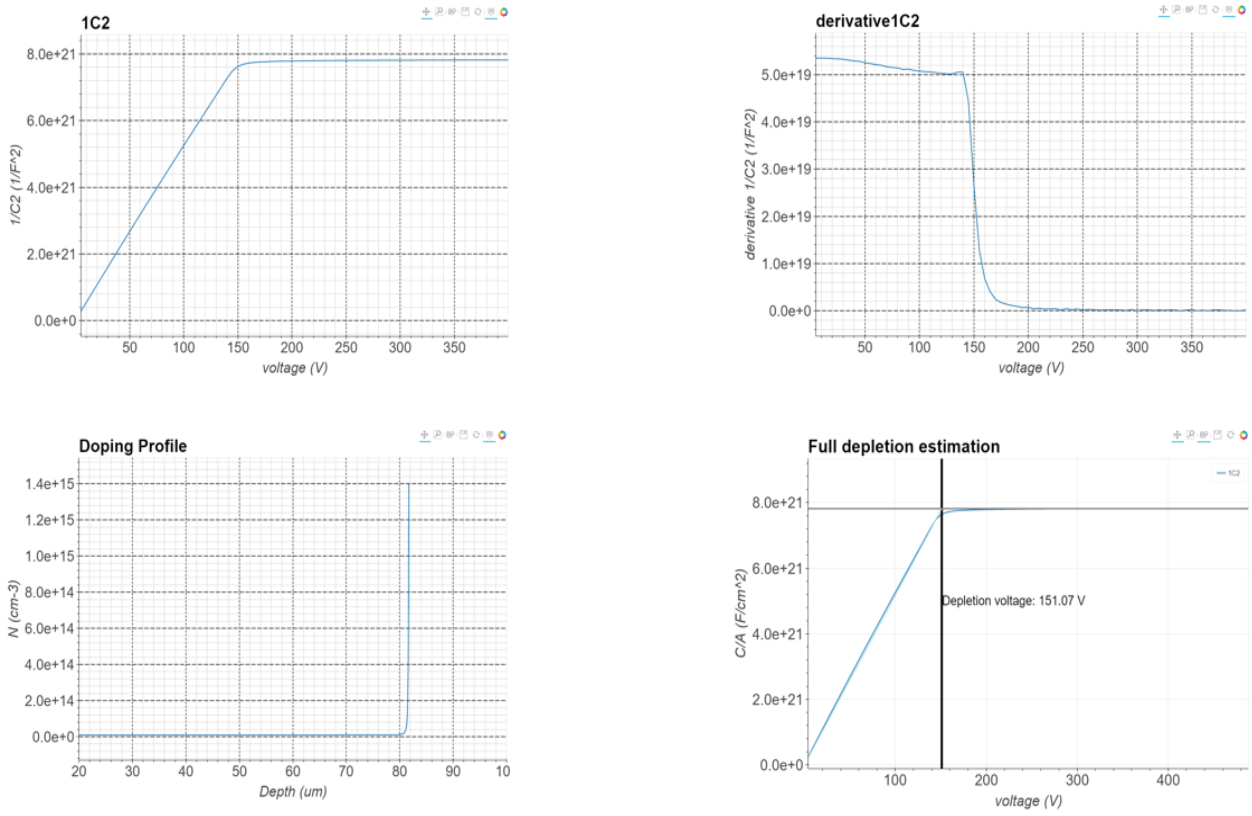


**Fig. 26.** Upper-left: $1/C^2$ curve. Upper-right: derivative of $1/C^2$. Lower-left: Doping profile. Lower-right: full depletion voltage estimation

## 4.4 MOS

A Metal-Oxide-Semiconductor (MOS) is utilized to trace a capacitance-voltage ($C-V$) characteristic curve, Fig. 27, and then determine the flat-band voltage from that, Fig. 28 - Fig. 29. Several MOS structures have been characterized in order to determine the flat-band voltage, $V_{\mathrm{fb}}$, fixed oxide charge concentration $N_{\mathrm{ox}}$, and oxide thickness $T_{\mathrm{ox}}$. This MOS structure features the same $SiO_2$ oxide layer as as the oxide layer atop the interstrip region of the sensors. The $V_{\mathrm{fb}}$ can be evaluated by finding the maximum value of the first derivative on the $C-V$ curve, the oxide capacitance $C_{\mathrm{ox}}$ can also be calculated considering the value of the capacitance measured in the accumulation region. For ideal curves, the flat-band voltage is 0 [27]. From the capacitance in accumulation $C_{\mathrm{ox}}$, the oxide thickness $T_{\mathrm{ox}}$ can be extracted using the standard parallel plate capacitor formula:

$$T_{\mathrm{ox}} = \epsilon_0 \, \epsilon_r \, \frac{A_{\mathrm{gate}}}{C_{\mathrm{ox}}} \tag{4.4}$$

where $A_{\mathrm{gate}}$ is the area of the gated electrode and with the relative permeability of $SiO_2$ being $\epsilon_r = 3.9$. The $V_{\mathrm{fb}}$ value can be calculated using :

$$V_{\mathrm{fb}} = \phi_{\mathrm{m}} - \phi_{\mathrm{s}} - \frac{Q_{\mathrm{ox}}}{C_{\mathrm{ox}}} \tag{4.5}$$

where $\phi_{\mathrm{m}}$ and $\phi_{\mathrm{s}}$ are the work functions of metal and semiconductor. The literature value for $\phi_{\mathrm{m}}$ of aluminum is of 4.08 $V$. The semiconductor work function $\phi_{\mathrm{s}}$ depends on the temperature $T$ and the doping density $N_{\mathrm{A}}$ and can be calculated for p-type material using:

$$\phi_{\mathrm{s}} = \chi - \frac{E_{\mathrm{g}}}{2} + \frac{k_{\mathrm{B}} \, T}{q} \ln\left(\frac{N_{\mathrm{A}}}{n_{\mathrm{i}}}\right) \tag{4.6}$$

where $\chi = 4.05$ eV is the electron affinity of silicon, $E_{\mathrm{g}} = 1.12$ eV is the energy of the bandgap in eV, $q$ is the elementary charge, $k_{\mathrm{B}}$ is the Boltzmann constant and $n_{\mathrm{i}} = 1.45 \,\mathrm{x}\, 10^{10}\,\mathrm{cm}^{-3}$ is the intrinsic doping concentration of silicon. The oxide charge concentration can be calculated using

$$Q_{\mathrm{ox}} = q \, N_{\mathrm{ox}} \, A_{\mathrm{gate}} \tag{4.7}$$

This leads to the oxide charge concentration [22] $N_{\mathrm{ox}}$:

$$N_{\mathrm{ox}} = \frac{C_{\mathrm{ox}}}{q \, A_{\mathrm{gate}}} \left(\phi_{\mathrm{ms}} - V_{\mathrm{fb}}\right) \tag{4.8}$$

where for an aluminum gate layer and p-type silicon with doping of $\sim 5 \,\mathrm{x}\, 10^{12}\,\mathrm{cm}^{-3}$ the work function difference $\phi_{\mathrm{ms}} = \phi_{\mathrm{m}} - \phi_{\mathrm{s}}$ is $\sim -0.68\,\mathrm{V}$. As can be seen in Listing 2, the MOS analysis script calculates the flat-band voltage using two different methods. The first one uses the maximum of the first derivative to find the flat-band voltage, Fig. 29. The second method uses the intersection between two linear fits, Fig. 28. The first fit considers the values between the minimum and the maximum of the second derivative, the other fit uses the values in the accumulation region. Then the analysis also finds accumulation capacitance, fixed oxide charge $N_{\mathrm{ox}}$ and oxide thickness $T_{\mathrm{ox}}$.

```
# Find the flatband-voltage through the maximum value of the first
    derivative
item_max = firstdev_interp.argmax()
voltage_value_of_max_firstder = xnew[item_max]
max_firstder_plot = hv.VLine(voltage_value_of_max_firstder).opts(
    line_width=1.0)
fbvoltage_firstderivative.append(voltage_value_of_max_firstder)

[...]

# Fit central region
for idx in range(indexMax, indexMin-1):
    # Do central fit
    slope_fit, intercept_fit, r_fit, p_valuefit, std_err_fit = linregress(
    df1["xaxis"][idx:indexMin-1],df1["yaxis"][idx:indexMin-1])
    r2_fit = r_fit * r_fit
    self.log.debug("central fit: Slope {}, intercept: {}, r^2: {}, std: {}
    ".format(slope_fit, intercept_fit, r2_fit, std_err_fit))

    # See if the r2 value has increased and store it
    if r2_fit >= fitR2:
        fitR2 = r2_fit
        fitEndPoints = ((df1["xaxis"][indexMax], slope_fit * df1["xaxis"][
    indexMax] + intercept_fit),
            (df1["xaxis"][idx+1], slope_fit * df1["xaxis"][idx+1] +
    intercept_fit)) # use idx +1 to avoid having the same end points
        fit_stats = [fitEndPoints, slope_fit, intercept_fit, r_fit,
    p_valuefit, std_err_fit]

# Add central slope
xmax = df1["xaxis"][indexMin]
fit_line = np.array([[df1["xaxis"][indexMax-3], fit_stats[1] * df1["xaxis"
    ][indexMax-3] + fit_stats[2]], [xmax+0.2, fit_stats[1] * (xmax+0.2) +
    fit_stats[2]]])

[...]


# Compute the flatband voltage
flatband_voltage = line_intersection(fit_stats[0], Right_stats[0])
self.log.info("Flatband voltage to data file {} is {}".format(df,
    flatband_voltage[0]))
```

**Listing 2.** Python code for MOS analysis. At first, the code computes the flatband voltage by means of the first-derivative. Then, it uses the intersection of two linear fits to compute again the flatband voltage. To achieve the best fits possible, the code search for the linear regression with the highest R-squared parameter.

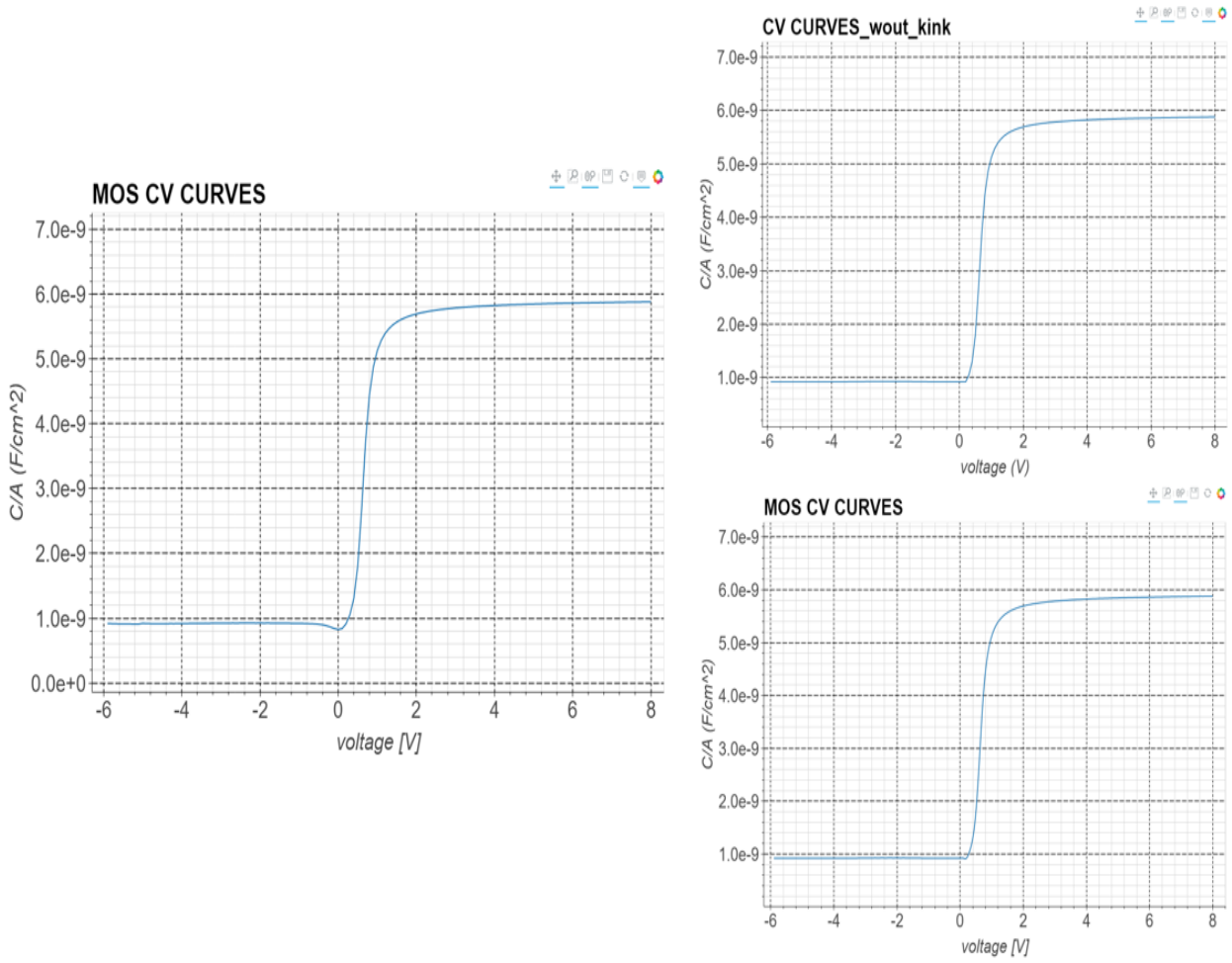


**Fig. 27.** Certain $C - V$ curves have a small undershoot (left) due to material-dependent characteristics of the non-ideal curve. This issue can be solved by averaging the capacitance values in the inversion region (upper-right) or by interpolation of the curve (lower-right).

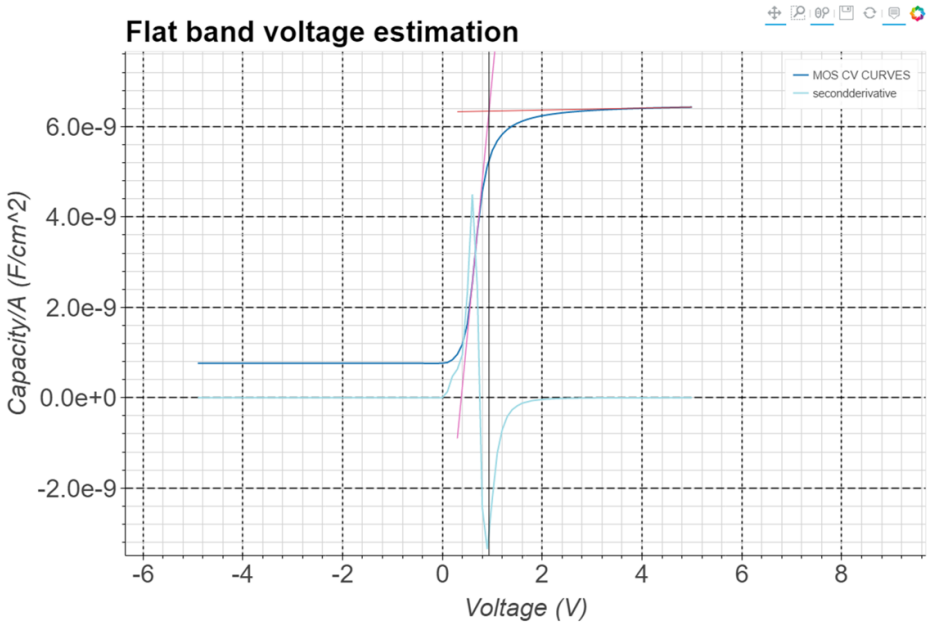


**Fig. 28.** Flatband voltage estimation by means of two linear fits. With this method, the flatband voltage is given by the intersection of a linear fit from the right (accumulation region) and a linear fit of the curve in the region between the two extrema of the second derivative (depletion region).

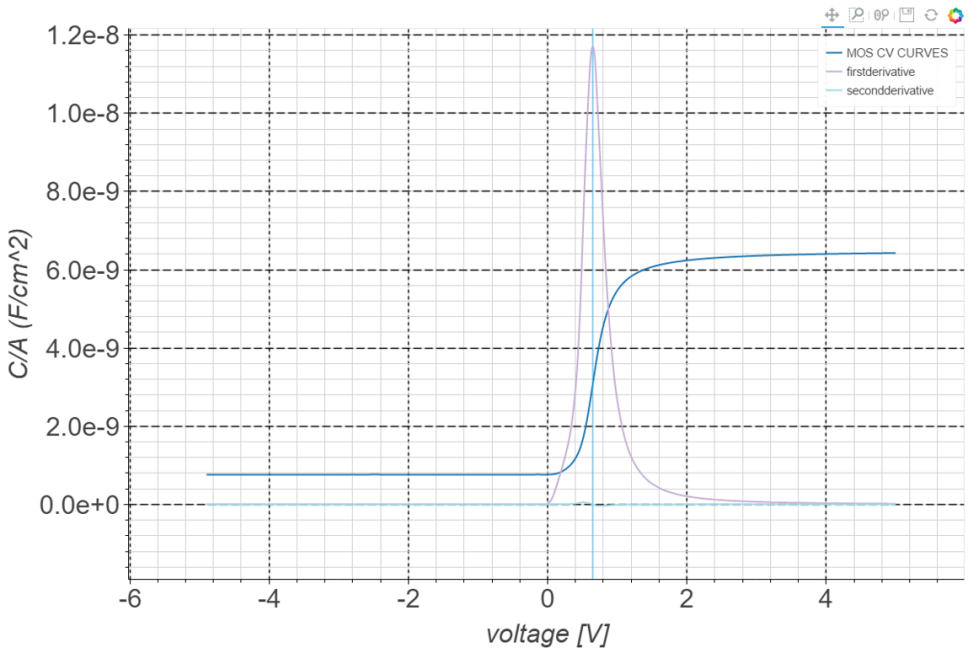


**Fig. 29.** Flatband voltage estimation by means of the first derivative. The flatband voltage is here the voltage value which corresponds to the maximum of the first derivative.

## 4.5 Gate Controlled Diode

The characteristics of the Gate Controlled Diodes (GCDs) are measured to determine the surface current $I_{\text{Surf}}$, and the surface recombination velocity $S_0$, which allow evaluating the quality of the Si-$SiO_2$ interface. From the diode current as a function of the gate voltage of a gated diode one can calculate $S_0$ using:

$$S_0 = \frac{I_{\text{Surf}}}{q\, A_{\text{gate}}\, n_{\text{i}}} \tag{4.9}$$

where $I_{\text{Surf}}$ is the difference between the current in depletion and inversion, $q$ is the elementary charge, $n_{\text{i}}$ is the intrinsic charge carrier concentration and $A_{\text{gate}}$ is the gate area. If the value of the surface current is high, one should suspect that oxide contamination issue took place in the course of the fabrication of the sensors and this could be problematic during irradiation, when more charges are introduced into the oxide layer.

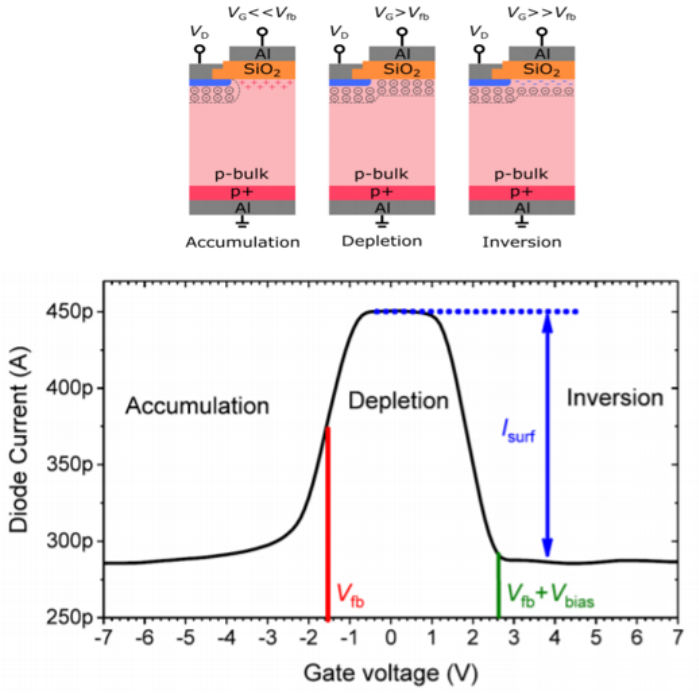


**Fig. 30.** Accumulation-depletion-inversion (Anreicherung-Verarmung-Inversion) regions (above) and typical GCD $I-V$ curve (below) [19]

As can be seen in Fig. 30, if a negative gate voltage is applied, for the case of accumulation, then the current $I$ consists only of the leakage current $I_{\text{bulk}}$ of the diode, which depends only by the extent of the depletion zone under the diode. If the gate voltage is increased until the flat-band voltage and beyond, the MOS structure also begins to deplete and merge with the depletion zone of the diode. The increase in current results both from the enlarged depletion zone around the MOS region $I_{\text{gate}}$ and from the recombination generation centers at the $\text{Si}-\text{SiO}_2$ boundary layer $I_{\text{Surf}}$. However, if the gate voltage reaches inversion, then the surface current contribution $I_{\text{Surf}}$ is separated again by the inversion layer and contributes no

more to the total current [9]. As shown in Listing 3, the GCD analysis script calculates the first and second derivative of the Current-Voltage curve in order to know where the depletion region is, Fig. 31. Then it calculates the surface current using two possible methods, Fig. 32. One simply considers the difference between the maximum of the $I-V$ curve and the mean value of the current in the inversion region. The other method considers the average of the current values in the depletion region and subtract this to the mean current value in the inversion region. Finally, it calculates the surface recombination velocity using (4.9).

```
# Interpolation current curve
xnew, ynew = self.interpolated_axis(df, self.data[df]["data"][self.xaxis],
    CurrentCopy)
curr_interp_plot = self.add_single_plots(xnew, ynew, "InterpolatedCurrent"
    )

# Build the first derivatives
firstderi_interp = self.build_first_derivative(xnew, ynew)
dif_intep_plot = self.add_single_plots(xnew, firstderi_interp, "
    FirstDerivativeCurrent")

# Second derivative
second_deriv_interp = self.build_second_derivative(xnew, ynew)
dif2_intep_plot = self.add_single_plots(xnew, second_deriv_interp, "
    SecondDerivativeCurrent")


# Compute the surface current with the average method
mxx = max(ynew)  # find maximum value of the current-voltage curve
miny = np.mean(list(ynew[-1000:]))  # find the minimum of the current-
    voltage curve by averaging 20 points values in the curve tail
I_surf_average = I_surf_maxima_average - miny  # compute the surface
    current by computing the difference between the maximum and minimum
    value
I_surf_average_table = '{:.2e}'.format(I_surf_average)
Surface_current_average.append(I_surf_average_table)

# Compute surface current with the maximum method
Isurf_max = mxx - miny  # compute the surface current by computing the
    difference between the maximum and minimum value
Isurf_table = '{:.2e}'.format(Isurf_max)
Surface_current.append(Isurf_table)
```

**Listing 3.** Python code for GCD analysis. At first, the code interpolates the data and then build first and second derivative in order to distinguish the depletion, accumulation and inversion region. Then, it computes the surface currents by averaging the current values in depletion, using the first method, or by finding the highest current value in depletion, using the second method.

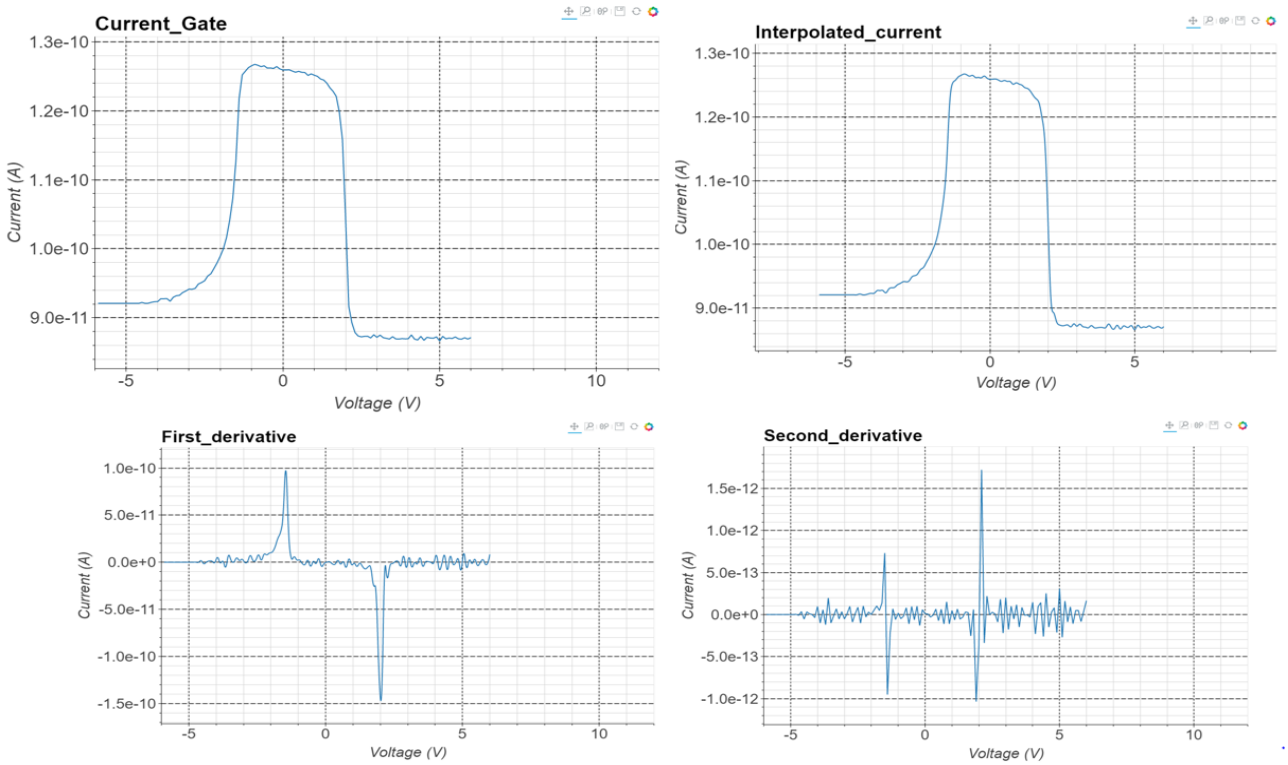


**Fig. 31.** Upper Right: Current-Voltage curve. Upper Left: Interpolation. Lower Left: first derivative. Lower Right: second derivative. The second differentiation usually introduces more noise.

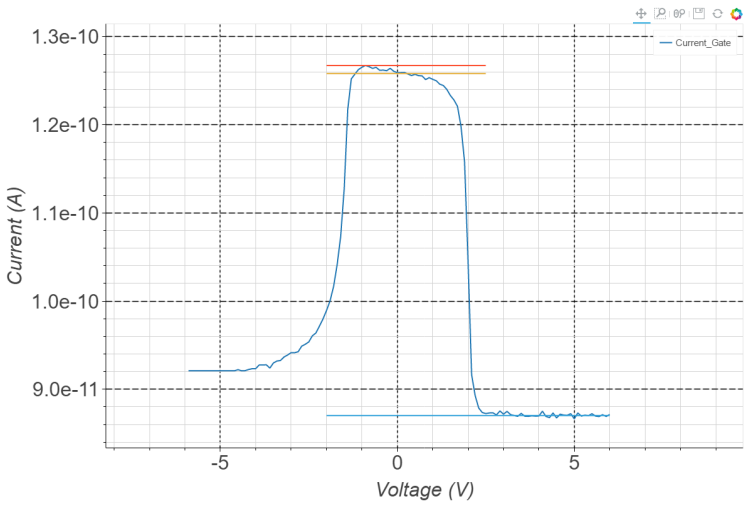


**Fig. 32.** The two methods to compute the current surface $I_{\text{Surf}}$: the average method (orange line), which requires computing the difference between the average of the current values in the depletion region (orange line) and the baseline of the plot (light blue). The max method, which involves computing the difference between maximum (red line) and baseline.

# 5 Summary and outlook

The Compact Muon Solenoid (CMS) is one of the detectors of the Large Hadron Collider LHC at CERN. After a shutdown phase, the CMS tracker will undergo an upgrade to be prepared for service during the High-Luminosity LHC (HL-LHC) era. In total, the CMS tracker and HGCAL system will consist of 50000 new silicon sensors occupying a total area of $800\,\mathrm{m}^2$. For a project of this magnitude, the CMS collaboration developed an elaborate design and a detailed quality assurance program to ensure the full compliance of all delivered sensors with the technical specifications. In this thesis, the emphasis was on "Process Quality Control" (PQC) to monitor the stability of the manufacturing process throughout the production phase. Using HEPHY's existing know-how, a working PQC analysis script has been developed to monitor the manufacturing process of the new CMS sensors. This has proven efficient to extract characteristic parameters. These are doping concentration and flat-band voltage for MOS structures; diode current ($I-V$), depletion voltage and resistivity ($C-V$) for Diodes; surface current for GCD structures. The future implementation of the PQC analysis software will also allow evaluating the systematic error and the characterization of the remaining test structures such as Metal-Oxide-Semiconductor Field Effect Transistors (MOSFETs), Van-der-Pauw Cross Structures, Cross Bridge Kelvin Resistance Test Structures, Contact Chain Test Structures, Dielectric Breakdown Test Structures and Meanders. This thesis has described the silicon sensors and shown the first results on PQC sensor qualification.

# References


[1] The Institute of High Energy Physics (HEPHY), URL https://www.oeaw.ac.at/en/hephy/the-institute/mission-statement, date of access: 19-06-2020.

[2] H. Hentschel, *MedAustron – Ionentherapie in Österreich*, DOI: 10.1055/s-0042-105815.

[3] F. Fayette, *Strategies for precision measurements of the charge asymmetry of the W boson mass at the LHC within the ATLAS experiment*, arXiv:0906.4260 [hep-ex].

[4] S. Bertolucci, The CERN Physics Programme, URL https://slideplayer.com/slide/129-49969, retrieved 19-06-2020.

[5] S. Chatrchyan, CMS Collaboration, *The CMS Experiment at the CERN LHC*, JINST 3 (2008) S08004, DOI: 10.1088/1748-0221/3/08/S08004.

[6] G. Perez, Unitarization Models For Vector Boson Scattering at the LHC, PhD Thesis, DOI: 10.5445/IR/1000082199.

[7] S. Matthias, *Review of single vector boson production in pp collision*, URL http://cds.cern.ch/record/1699952/plots.

[8] CMS collaboration, URL http://cms.cern/detector/identifying-tracks, retrieved 19-06-2020.

[9] H. Kolanski, N. Wermers, *Teilchendetektoren: Grundlagen und Anwendungen*, DOI: 10.1007/978-3-662-45350-6.

[10] S. Solomon, *Measurement of the Production Cross-Section of the Z Boson and Determination of its Spin with the ATLAS Detector*, URL: https://cds.cern.ch/record/2667047.

[11] HL-LHC industry, URL https://project-hl-lhc-industry.web.cern.ch/content/project-schedule, retrieved 18-08-2020.

[12] D. Contardo, M. Klute, J. Mans et al., *Technical Proposal for the Phase-II Upgrade of the CMS Detector*, Tech. Rep. CERN-LHCC-2015-010, LHCC-P-008, CMS-TDR-15-02, CERN, Geneva, 2015, URL: http://cds.cern.ch/record/2020886.

[13] L. Mastrolorenzo, 21st Particles and Nuclei International Conference (PANIC 2017), International Journal of Modern Physics: Conference Series Vol. 46 (2018) 1860075 (6 pages), DOI: 10.1142/S2010194518600753.

[14] T. Bergauer, *Design, Construction and Commissioning of the CMS Tracker at CERN and Proposed Improvements for Detectors at the Future International Linear Collider*, URL: https://cds.cern.ch/record/1444582/files/diss.pdf.

[15] W. R. Leo, *Techniques for Nuclear and Particle Physics Experiments*, Second Revised Edition, Springer-Verlag Berlin Heidelberg GmbH.

[16] V. Hinger, *Charge Sharing Studies of Silicon Strip Sensors for the CMS Phase II Upgrade*, Master thesis, TU Wien.

[17] Microchemicals GmbH, Silicon Ingot Production: Czochralski- and Float-Zone Technique, URL: https://www.microchemicals.com/products/wafers.html, retrieved 1-06-2020.

[18] V. Hinger on behalf of the CMS Collaboration, *Process quality control strategy for the Phase-2 Upgrade of the CMS Outer Tracker and High Granularity Calorimeter*, arXiv:2003.11092.

[19] V. Hinger, Specifications and procedures for the CMS Outer Tracker Process Quality Control.

[20] J. Agram, M. Angarano, S. Assouak et al., *The Silicon Sensors for the Compact Muon Solenoid Tracker - Design and Qualification Procedure*, CMS NOTE 2003/015.

[21] F. Moscatelli, A. Rossi, V. Mariani, et al., *Preliminary report on Pre-seriesTest structures.*

[22] A. Koenig, *Planar Silicon Strip Sensors for the CMS Phase Phase-2 Upgrade*, PhD thesis, TU Wien.

[23] R. Dallavalle, PQC analysis script, URL https://github.com/Chilldose/COMET/blob-/master/COMET/misc_plugins/PlotScripts/analysis_scripts/IV_PQC.py.

[24] D. Blöch, B. Arnold, COMET, URL https://github.com/Chilldose/COMET

[25] R. Dallavalle, PQC parameters script, URL https://github.com/Chilldose/COMET/blob/master/COMET/config/Setup_configs/DataVisualization/Plotting/PQC_IV.yml.

[26] R. Dallavalle, PQC importer, URL https://github.com/Chilldose/COMET/blob/master/COMET/misc_plugins/PlotScripts/importer/importer_PQC.py.

[27] Dieter K. Schroder, *Semiconductor Material and Device Characterization*, Third Edition, DOI:10.1002/0471749095.